UNIVERSITY OF OKLAHOMA

GRADUATE COLLEGE

MODELING ADSORPTION IN SHALE

A THESIS

SUBMITTED TO THE GRADUATE FACULTY

in partial fulfillment of the requirements for the

Degree of

MASTER OF SCIENCE

By

YULIANA MARIA ZAPATA ARBOLEDA
Norman, Oklahoma
2016

MODELING ADSORPTION IN SHALE

A THESIS APPROVED FOR THE
MEWBOURNE SCHOOL OF PETROLEUM AND GEOLOGICAL ENGINEERING

BY

_____
Dr. Ahmad Sakhaee-Pour, Chair

_____
Dr. Maysam Pournik

_____
Dr. Mashhad Fahs

To my parents, Ana and Jaime, and my sister Laura for being my fuel.

Acknowledgements

I would like to express my deepest gratitude and appreciation to my advisor Dr. Ahmad Sakhaee-Pour for his expertise, motivation and continuous support. His guidance helped me throughout the research.

To the members of my thesis committee, Dr. Mashad Fahs and Dr. Pournik, I am extremely grateful for your suggestions and help, specially during the last stages of my studies. Furthermore, I would like to thank the Mewbourne School of Petroleum and Geological Engineering staff for their valuable assistance and support.

Finally, I would like to thank my family, my friends Andres Alzate, Ricardo González, Elizabeth Arias, and specially Saurabh Sinha for always being there to encourage me.

Table of Contents

List of Tables

List of Figures

Abstract

The existing conventional methods to characterize reservoir storage properties face challenges in shale formations due to their fine grained texture, low porosity, and low permeability. An integrated analysis of standard core measurements, such as adsorption-desorption isotherms and mercury intrusion capillary pressure, helps us to better understand these formations by determining the pore size that controls the stored volume and flow conductance at a larger scale.

We propose a new model to distinguish and characterize the pore-body and pore-throat size distributions for the connected pore space of shale formations. We simultaneously analyze different sorption mechanisms such as multilayer adsorption and capillary condensation for nitrogen adsorption-desorption isotherms to determine the pore-body size. By accounting for the coupled processes, we predict the amount of gas adsorbed in the studied core samples. The model provides an explanation for the gas storage behavior at the core scale that can be extended to assess the formation. We also analyze mercury intrusion data not to validate the pore-body size obtained from nitrogen adsorption but to determine the pore-throat size. The integrated analysis of these measurements enables us to fully characterize the pore space of a shale formation.

Chapter 1: Introduction

1.1. Problem Statement

Shale plays recently became relevant in the energy market, when profitable gas production from these low-permeability formations turn into a reality. Particularly, in the U.S. large-scale production of shale gas started around 2000 in north-central Texas from the Barnett formation after energy companies successfully experimented with different hydraulic fracturing techniques. Further, Exploration and production were extended to additional shale plays (Fayetteville, Haynesville, Woodford, Eagle Ford, and others) in the country as the knowledge and ability to commercially develop the formations increased. By the end of July 2016 the dry gas production from shale formations in the U. S. reached 41.8 bcf per day. (U.S. Energy Information Administration, 2016).

Understanding the storage and transport properties of shale formations is required to successfully develop its resources. However, determining petrophysical properties of interest like porosity and permeability turned out to be a challenge given that they can be significantly different from conventional formations. These formations exhibit significant low permeability and porosity that have been related to the presence of narrower pores and poor connectivity between them. Many studies have been conducted to analyze the pore structure of shale, shedding light on the complexity of its pore space.

1.2. Objective

Our objective is to determine the pore-body size and the pore-throat distributions for different shale samples, as a mean to understand the storage capacity and the transport behavior in this type of formations. We characterize the pore space of a shale to determine the pore-body size distribution by capturing nitrogen adsorption-desorption based on the acyclic pore model. We also calculate the pore-throat size distribution via analyzing mercury intrusion capillary pressure measurements. We will compare the results to highlight the difference between the two sizes for shales.

1.3. Hypothesis

If we account for the adsorbed volume at pore scale using appropriated adsorption mechanisms (multilayer adsorption, capillary condensation, and others) based on the acyclic pore model, we can capture the nitrogen (N_2) adsorption-desortion hysteresis and characterize the pore structure for shale.

Chapter 2: Literature Review

2.1. Adsorption

The term adsorption refers to the process of accumulation of fluid (adsorbate) onto a solid surface (adsorbent). When a solid surface is exposed to a gas, its molecules may stick to the surface increasing the concentration of gas in the neighboring area for a finite amount of time.

The amount of gas adsorbed at any time is a function of the interaction between the solid and the gas, as well as other properties of the system The nature of the interactive forces between the adsorbent and the adsorbate determine whether the adsorption is physical or chemical. Physical adsorption or physisorption occurs when the interaction is weak and the process is easily reversed using heat or decreasing the pressure, and chemical adsorption or chemisorption occurs when the attraction between the solid and the molecules adsorbed is strong creating chemical bonding (Graf & Kappl, 2003).

2.1.1. Adsorption in porous solids

For porous solids, the size of the pores and the connections among them are important in the context of adsorption. The pore sizes are classified following the IUPAC (International Union of Pure and Applied Chemistry) definitions as shown in Table 1. In particular, for micropores and mesopores the adsorption-desorption of gas molecules is an important mechanism of storage, given that the pore size is comparable to the molecules size and the adsorbed layer thickness (Boucher, 1976).

Table 1. Pore size classification according to IUPAC (International Union of Pure and Applied Chemistry). For micropores and mesopores the amount of gas adsorbed is significant given that the pore size is comparable with the adsorbed molecules or adsorbed layer size.

Term	Pore Size Range
Micropore	Less than 2 nm
Mesopore	2 nm -50 nm
Macropore	Greater than 50 nm

The adsorption process can take place through a series of mechanisms that differ in nature and are dependent on the pore size and other properties of the system like pressure and temperature. For instance, for micropores where the size of the pore is close to the size of the gas molecules the adsorption forces are higher than for larger pore sizes, thus the adsorption process occurs at lower pressures and is considered continuous due to stronger interactions between the porous solid and the gas. This type of adsorption has been called volume filling of micropores or micropore primary filling (Dubinin, 1989).

For mesopores, which are nanoporous materials typical sizes, the main adsorption mechanisms are: monolayer adsorption, multilayer adsorption and capillary condensation. Figure 1 depicts these adsorption mechanisms for a slit like pore as pressure increases. In (a) the gas molecules are adsorbed occupying the available sites on the pore surface and forming a monomolecular layer. The monolayer will attract other gas molecules, thus the layer adsorbed becomes several molecules thick forming a multilayer as shown in (b). At certain pressure, the thickness of the adsorbed layer

becomes close to the size of the pore and the gas molecules condensate inside it. This process is known as capillary condensation (Roque-Malherbe, 2007).

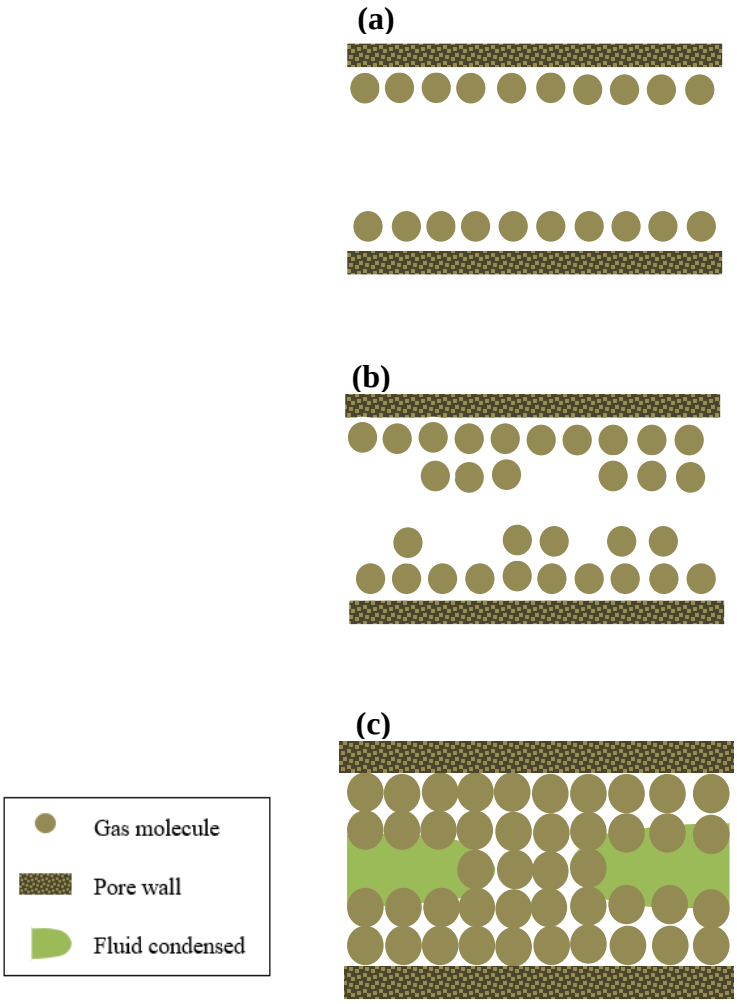

Figure 1. Adsorption stages inside a pore (a) formation of a monolayer, (b) gas molecules get attached onto the monolayer, creating a multilayer, and (c) fluid condensation starts inside the pore when the thickness of the adsorbed layer is close to the pore size, this is known as capillary condensation (Roque-Malherbe, 2007).

The different adsorption mechanisms can also be identified on the adsorption isotherm where the amount of gas adsorbed (n_a) is plotted against the relative pressure (P/P_o). Figure 2 is a sketch of the nitrogen adsorption isotherm for a single pore. An adsorbed layer begins to form on the walls, the slope of the curve is steep in this region as the molecules adhere directly onto the surface of the pore. The layer gets thicker during the multilayer adsorption, during this stage the amount of gas adsorbed does not increase as fast with increasing pressure as during the monolayer adsorption, resulting in a gentle slope. When the condensation pressure for the given pore size is reached and the gas molecules turn into a liquid like phase inside the pore, the amount adsorbed increases instantly and reaches a plateau-like stage (Seaton, 1994).

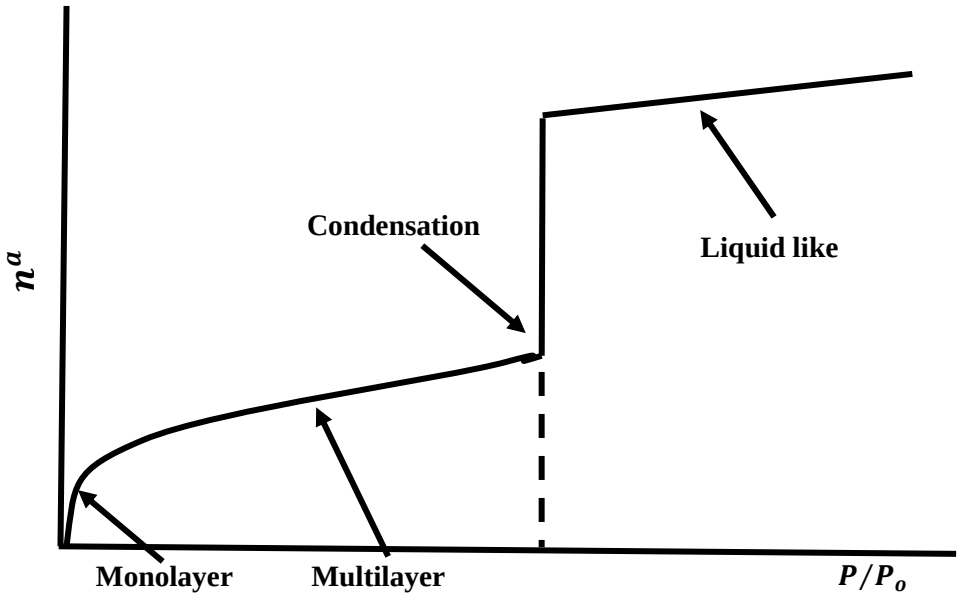

Figure 2. Adsorption isotherm for a single pore, where n_a is the amount adsorbed and P/P_o is the relative pressure. The isotherm Different adsorption stages or mechanisms can be observed in the curve. relation between each mechanism and From (Seaton, 1994).

The thickness of the layer formed during monolayer or multilayer adsorption is an important parameter that can be used to calculate specific surface area of the pores and pore size distribution analysis (Everett et al., 1985). In 1966 De Boer et al., defined the t-curve, which allows to calculate the thickness of the adsorbed layer as a function of the relative pressure. Other theoretical and empirical models have been developed to account for the layer adsorbed in porous solids (Halsey, 1948; Jura & Harkins, 1943).

2.1.2. Amount of gas adsorbed

The amount of gas adsorbed is a function of the equilibrium pressure of the gas at which adsorption takes place, the temperature, the nature of both the solid and the molecules of the gas adsorbed, and the surface area of the solid (Rouquerol, Rouquerol, Llewellyn, Maurin, & Sing, 2013). For a given gas adsorbed on a particular solid at a constant temperature below its critical temperature, the amount of gas adsorbed can be expressed as in Equation (1)

$$\frac{n^a}{m^s} = f\left(\frac{P}{P_o}\right)_T \tag{1}$$

where n^a is the amount adsorbed, m^s is the mass of solid, P is the gas pressure, P_o is the saturation pressure at T, and T is the temperature.

The quantity of gas adsorbed can be express as the mass of gas, the amount of gas molecules, gas moles or the volume of gas. Is common practice to use the unit STP cc/g, which indicates the amount of gas adsorbed, measured in cubic centimeters at standard temperature and pressure conditions per gram of adsorbent (solid). These units are useful given that the methods used to determine the adsorption isotherm experimentally mostly

imply the measurement of the volume of gas adsorbed for a certain amount of solid sample, while pressure is change (De Boer, Broekhoff, Linsen, & Meijer, 1967).

2.2. Adsorption isotherms

An adsorption isotherm is the graph of the amount of gas adsorbed versus the relation of the pressure of the vapor phase and its saturation pressure (P/P_o), known as relative pressure. In 1985, IUPAC (International Union of Pure and Applied Chemistry) classified the adsorption isotherms for different gas-solid systems into six types shown in Figure 3.

Type I is known as the Langmuir isotherm and it is related to the formation of one single layer (monolayer adsorption) in microporous solids. The curve exhibits a plateau (limiting value) that represents the maximum capacity of adsorption, which depends on the accessible micropore volume (Everett et al., 1985).

Type II and III represent non-porous or macroporous adsorbents, which allow unrestricted formation of layers at high pressures (i.e. no plateau is observed). The main difference between type II and III is the fluid-wall attractive forces, which are strong for type II and weak for type III. Types I, II and III are all known as reversible isotherms given that the adsorption and desorption curves follow the same path, meaning there is no hysteresis when the pressure is reduced (Graf & Kappl, 2003; Rouquerol et al., 2013).

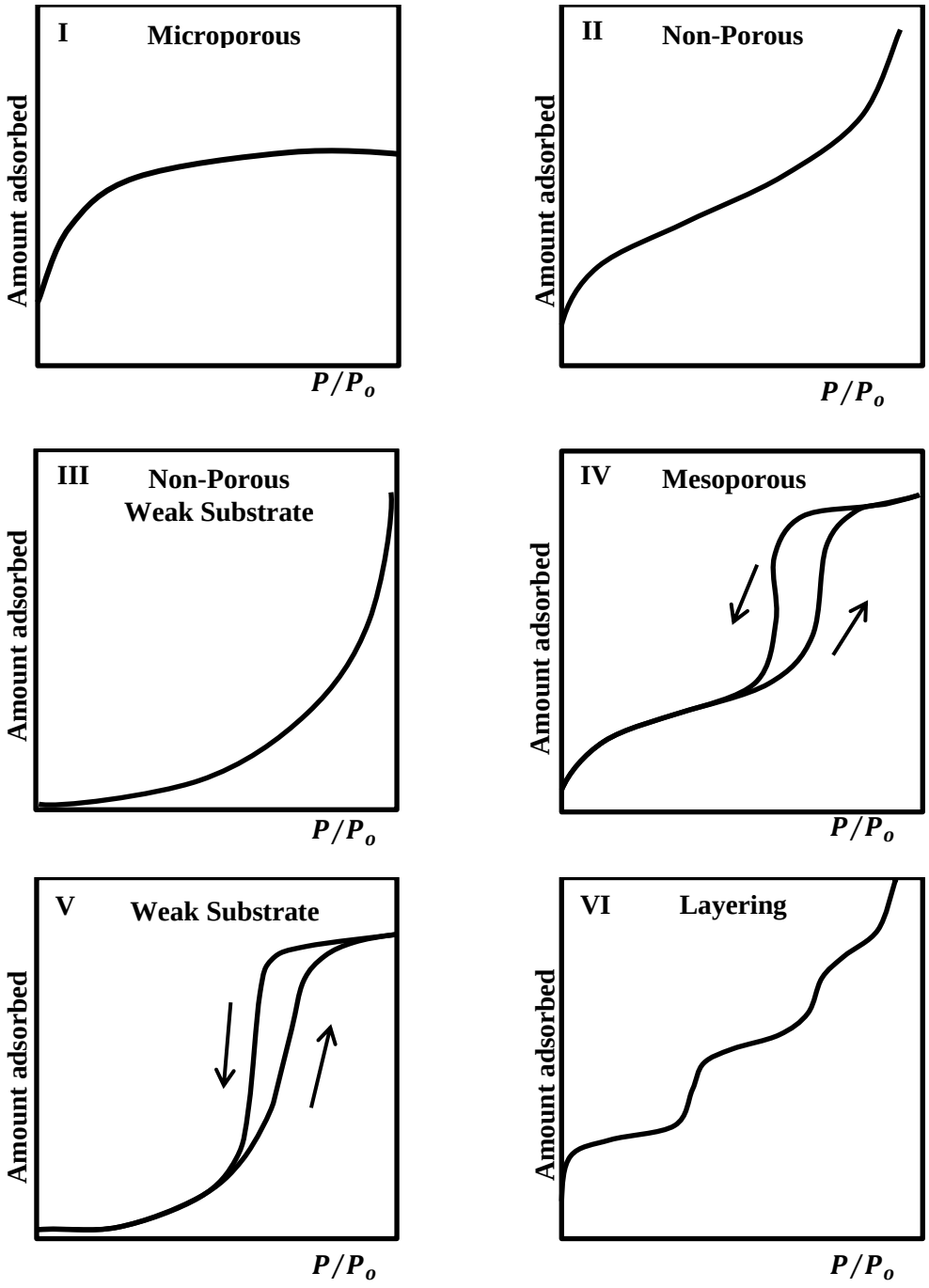

Figure 3. Adsorption isotherms types according to IUPAC (International Union of Pure and Applied Chemistry). The amount of gas adsorbed against the relative pressure reflects the relation between the solid (adsorbent) and the gas (adsorbate), as well as structural characteristics of the solid.

Type IV is characteristic of solids with mesopores. It exhibits a hysteresis loop (different paths for adsorption and desorption can be noticed), that can be explained by the effect of pore blockage during the emptying of the pores, or by the capillary condensation process. Type V also exhibits hysteresis loop and is characteristic of solids with pore sizes within the mesopore range. The main difference with type IV is the fluid-wall forces, which are strong for IV and weak for V. Finally, type VI or stepped isotherm is associated with layer-by-layer adsorption on uniform surfaces (Balbuenat & Gubbins, 1993; Rouquerol et al., 2013)

2.2.1. Langmuir Isotherm

The equation most frequently used to describe the adsorption of gas on solids is the Langmuir isotherm due to its simplicity even though is not appropriate for every adsorption mechanism. Also known as type I isotherm according to IUPAC as shown in Figure 3. Langmuir's equation is based on the following main assumptions (Langmuir, 1918):

(a) Only a single layer of gas molecules can cover the surface

(b) The gas behaves as an ideal gas

(c) The adsorbed molecules do not affect the molecules on the neighboring site (no repulsion)

(d) The surface has a specific number of sites where molecules can be adsorbed

Langmuir equated the rate of molecules being adsorbed on the surface with the rate of molecules leaving the adsorption sites (evaporating from the surface) to finally obtained Equation (2):

$$V = V_m \frac{P}{P_L + P} \tag{2}$$

where V is the volume of gas adsorbed (m^3/g of adsorbent), V_m is the Langmuir volume (Volume of gas adsorbed when the entire surface is covered by a monolayer), P pressure(N/m^2), and P_L is the Langmuir pressure (adsorption equilibrium constant).

2.2.2. BET isotherm

Brunauer, Emmett, & Teller (1938) derived an equation of the isotherm for multilayer adsorption, based on the equation developed previously by Langmuir. The main assumptions of their theory are:

(a) Gas molecules can be adsorbed in layers infinitely (multilayer adsorption)

(b) There is no interaction between layers

(c) Langmuir equation can be applied to each layer

(d) The energy of adsorption is the same for all the layers (heat of condensation), except the first one (heat of adsorption)

The S-shaped isotherm equation (Equation (**3**) consists of two regions: the low pressure region that is concave to the pressure axis, and the high pressure region where the curve becomes convex. Given the shape obtained, the adsorption curves from Types II, IV and VI from IUPAC classification (see Figure 3) can be captured by the BET isotherm.

Furthermore, the temperature dependence for c and v_m can be described (Brunauer, Deming, Deming, & Teller, 1940).

$$v = \frac{v_m c P}{(P_o - P)[1 + (c - 1)(P/P_o)]} \quad (3)$$

where v is the volume of gas adsorbed at pressure P, V_m is the volume of gas adsorbed in one complete monomolecular layer (monolayer), c is a constant dependent on the energy of adsorption and condensation, P is the gas pressure and P_o is the saturation pressure of the bulk fluid (gas). This can be rewritten in a convenient form, with the intention of obtaining a plot of $[P/v(P_o - P)]$ against $[1/v_m c]$ that gives a straight line, whose intercept and slope can be used to evaluate v_m and c (Brunauer et al., 1938).

2.3. Hysteresis

Adsorption in porous materials is often characterized by hysteresis when the process is reversed (i.e. during desorption). The behavior observed while the pressure is being increased differs from the behavior when it is reduced. In other words, as the vapor pressure decreases, desorption occurs at a pressure lower than the pressure of adsorption. Hysteresis can be observed in single pores as well as in pore networks (Seaton, 1994).

The hysteresis loops are associated with capillary condensation, due to the difference of pressures between condensation and evaporation. Besides this thermodynamic mechanism, hysteresis also depends on the connectivity of the pores within the pore network, the spatial distribution and the connection with the surface. During desorption, vaporization can occur only from pores that have access to the vapor phase, and not from

pores that are surrounded by other liquid-filled pores. This is known as the pore blocking effect (Donohue & Aranovich, 1998; Naumov, 2009).

2.3.1. Hysteresis loop types

Hysteresis loops were classified by IUPAC in 1985 into four types as shown in Figure 4. Relevant characteristics of the hysteresis loop are the width of the loop which is temperature (shrinks as temperature increases) and pore structure dependent, and the lower closure point that is the pressure at which the adsorption and desorption branches are equal at lower pressures. The closure point is generally independent from the nature of the porous adsorbent but depends mostly on the nature of the fluid being adsorbed (i.e. the gas), for example for nitrogen at 77 K the closure point is at $P/P_o \approx 0.42$ (Everett et al., 1985).

In type H1 both the adsorption and desorption branch are steep at intermediate relative pressures, it is related to porous materials of relative uniform capillary tubes open at both ends. Type H2 loop is broad with long-flat plateau, the desorption branch is steep at intermediate relative pressures. It is associated with ink–bottle shaped pores and complex pore structures. For type H3 loop the adsorption branch is steep at the saturation pressure, the desorption branch is steep at intermediate relative pressures and does not exhibit any limiting adsorption at high relative pressures. It is related to open slit-shaped pores or plate like particles. Type H4 loops do not terminate in plateau and are also given by slit-shaped pores, they are observed in complex materials containing both micropores and mesopores (Sing & Williams, 2004; Thommes, 2010).

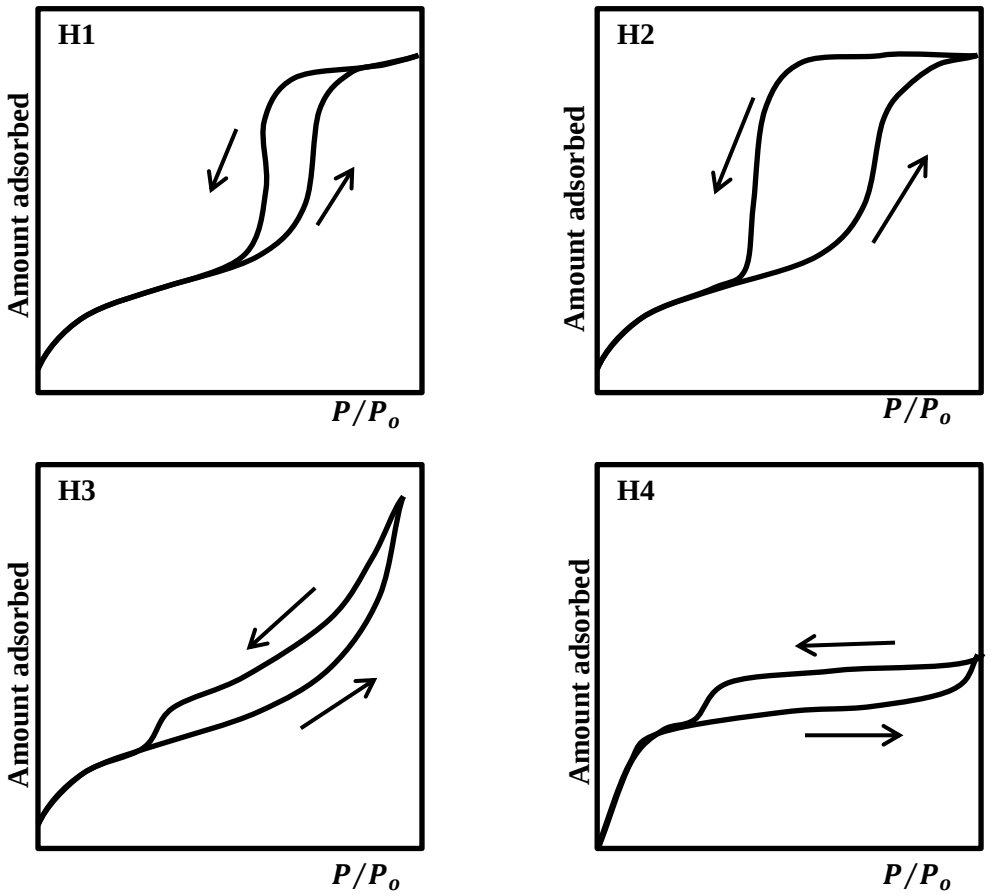

Figure 4. Types of hysteresis loop according to IUPAC's classification. The hysteresis shape is associated with capillary condensation, the connectivity of the pores within the pore network, the spatial distribution and the pore connection with the surface.

2.4. Capillary condensation

When a fluid is confined inside pores with sizes within the mesopore range, it condenses at pressures lower than the saturation pressure of the bulk fluid at a given temperature. This phenomena is known as capillary condensation, the pressure at which condensation occurs is a function of the pore size, shape, and the interaction between the fluid and pore walls (Gubbins, Long, & Śliwinska-Bartkowiak, 2014).

During adsorption, multiple layers of adsorbed gas first cover the pore walls until a certain critical thickness is reached and the condensation occurs in the core of the pore, controlled by intermolecular forces in the core fluid (Boucher, 1976). The equations used to describe this mechanism are the Kelvin equation and the Kevin-Cohan equation.

2.4.1. Kelvin equation

The Kelvin equation gives the pores size as a function of the relation of the gas pressure (P) at which condensation occurs inside the pore and the saturation pressure (P_o) of the bulk fluid, this is relation is called relative pressure. The Kelvin equation (Equation 4) is only valid for the mesopore range, where the capillary condensation phenomena is relevant, it does not apply to macropores or micropores (Skinner & Sambles, 1972)

$$r_K = \frac{-2\gamma\, V_{mol} \cos\theta}{RT ln\left(\frac{P}{P_o}\right)} \tag{4}$$

In Equation (4) r_K is the radius of the pore in which condensation occurs (m), γ is the surface tension of the liquid adsorbate (N/m), V_{mol} is the volume occupied by 1 mole of condensate at T (m^3/mol), θ is the contact angle between the liquid and the pore wall, R is the gas constant (8.314 J/Kmol), T is the temperature in Kelvin, P is the pressure of condensation inside the pore (N/m^2) and P_o is the saturation pressure of the bulk fluid.

Capillary condensation is directly related with the hysteresis loop between the adsorption and desorption curves for pores wider than approximately 5 nm (mesopores). This means

that, as the vapor pressure decreases, desorption occurs at a pressure lower than the pressure of adsorption due to the difference between the capillary condensation and evaporation. (Rouquerol et al., 2013)

2.4.2. Kelvin-Cohan equation

Kelvin equation ignores the fact that adsorption inside the pores is not only given by capillary condensation. In order to account for all the fluid adsorbed by other mechanisms for instance multilayer adsorption, it is necessary to include the gas previously adsorbed on the pore walls. The Kelvin-Cohan or modified Kelvin equation is derived from the Kelvin equation, which is based on the effect of the curvature of the surface on vapor pressure, and includes the thickness of the adsorbed layer. Along with distinguishing between adsorption and desorption (Cohan, 1938).

The Kelvin-Cohan equation is based on the assumption that the kelvin radius (Equation 4) is not going to be equal to the pore radius given that some gas has already been adsorbed on the pore walls as shown in Figure 5. Then, the pore radius can be written as in Equation (5):

$$r_p = r_k - t \tag{5}$$

Where r_p is the porous radius, r_k is the kelvin radius and t is the thickness of the adsorbed layer.

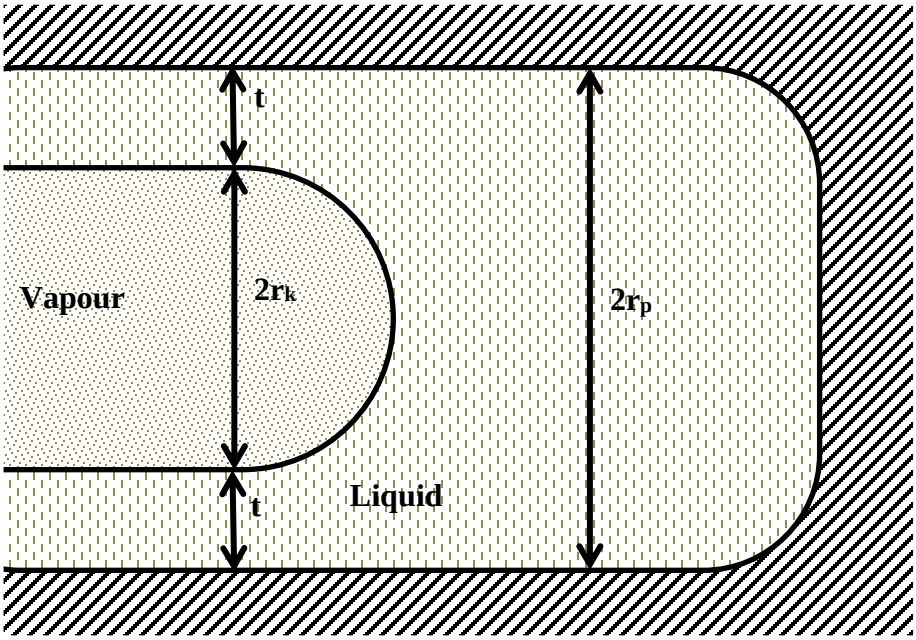

Figure 5. Relationship between the Kelvin radius and the pore radius in a cylindrical pore. Based on (Cohan, 1938).

2.5. Pore size distribution from adsorption isotherms

Using experimental adsorption isotherms for porous solids, it is possible to obtain the pores size distribution (cumulative pore volume vs. pore radius) of the samples analyzed based on a selected model that represents the pores structure and state. The geometrical structure of a single pore (unit) can be considered cylindrical, ink bottle, slit-shaped, etc. The pore state may vary from open pores which are communicating with an external surface, or closed pores with restricted access for molecules and without communication to the surroundings (Kaneko, 1994)

The procedures to determine the pore size distribution, describe an algorithm that gives the volume and surface area contained in a group of pore sizes using either the adsorption

or desorption branch measurements. Usually, the techniques developed use nitrogen as the adsorbate for the isotherm measurements and are based on a cylindrical pore shape. Many investigators use both, multilayer adsorption and capillary condensation to describe the adsorption-desorption proccess. Following, a brief description of three commonly use the existing models: Barrett-Joyner-Halenda, Cranston-Inkley method and Modelless method.

2.5.1. Barrett-Joyner-Halenda method

The BJH method was developed in 1951 by Barrett, Joyner and Halenda. It estimates the volume and area of porous adsorbents with a wide range of pore sizes. The model is a system of open ended, cylindrical pores. The radii of the pores are given by the kelvin radius r_k and the thickness of the adsorbed layer t, given by the t-curve developed by Schull (1948). It is based on the combined mechanisms of physical adsorption and capillary condensation. The pore volume and area distribution are directly computed from the desorption branch isotherm (Barrett, Joyner, & Halenda, 1951).

2.5.2. Cranston-Inkley method

The pore structure analysis proposed by Cranston and Inkley in 1957, can be made for either the adsorption or desorption branch of the isotherm. Initially, it assumes the pores are cylindrical and one end closed. The pore sizes are divided into groups with a given average radius r_p. All pores with radii larger than r_p contained an adsorbed layer of thickness t given by t-curve based on Hasley's equation (Halsey, 1948). For the pores

smaller than r_p, the pores are filled following both the multilayer adsorption and capillary condensation theories (Cranston & Inkley, 1957).

2.5.3. Modelless method

It is called modelles method because it does not assume any pore shape for the pore structure analysis. It is based on the hysteresis of the adsorption-desorption isotherms, the region where both multilayer adsorption and capillary condensation can occur. The pore volume and the surface area distribution are determined as a function of the hydraulic radius (unlike other methods based on Kelvin radius). This method is only applicable for wide pores, to analyze the structure of micropores it is necessary to use an alternate method (Brunauer, Mikhail, & Bodor, 1967).

2.6. Pore structure modeling for rock formations

Accounting for the interactions and distribution of pores in the rock is very important to understand the flow through a formation, given that the topology of the pore space controls its transport properties. Pore structure modeling refers to the theoretical study and analysis of the rock structure at pore-scale to represent and capture the space characteristics (Bryant, Mellor, & Cade, 1993; Mousavi & Bryant, 2012).

In general, a rock formation contains solid grains (non-void regions) and pores (void regions). The void space can be divided into pore-bodies and pore-throats to allow the analysis of interactions between the pores. The pore throat is the narrowest region of the pore space connecting the neighboring pores and has a dominant effect on the fluid

displacement (the interaction between the pores occurs through the pore throats), whereas the pore body is the wider region of the pore (Sakhaee-Pour & Bryant, 2015).

To determine the pore-throat size distribution for the connected path of the pores at the core scale, we often analyze the drainage data, in which the non-wetting phase displaces the wetting phase. The invasion percolation suggests that the invading fluid displaces the resident fluid when the applied capillary pressure is larger than the critical pressure for the connecting throat. The critical capillary pressure is a function of the throat curvature that can allow us to determine the pore-throat size distribution using Young-Laplace relation (Kate & Gokhale, 2006; Purcell, 1949; Swanson, 1981; Washburn, 1921).

On the other hand, the pore-body size governs the bulk pore volume. To evaluate pore-body size distribution, the adsorbed volume from adsorption-desorption isotherm is analyzed (as described in section 2.5). Obtaining a representative pore size from the pore-throat and the pore-body sizes analysis is very important, because it allows us to derive a network of the connected pores that can be used for analyzing transport properties at the core scale (Ovaysi, Wheeler, & Balhoff, 2014).

2.6.1. Existing models

Theoretical pore models that account for the effective pore connectivity at the core scale include: bundle-of-tubes, regular lattice, sphere packing, multi-type model, and acyclic pore model. These models represent the pore space because they can capture the transport properties at the core scale. Another aspect of fluid flow through porous media is the

linkage between core-scale and field-scale properties. Study conducted by Frooniqa 2014, introduced a new method that, for the first time, quantified field-scale pore connectivity and formation permeability using production logs. Their physics-based model makes it possible to estimate the sensitivity of production data to core-scale formation properties (Frooqnia et al., 2013; Frooqnia et al., 2016a). This approach opens a new window for constructing an accurate reservoir flow model, which is essential for calibration of pore- and core-scale reservoir properties (Frooqnia et al. 2016b). Another application is to quantify fracture network connectivity based on simulation and robust inversion of single-phase production logs (Frooqnia et al., 2011).

2.6.1.1. Bundle-of-tubes

The void space is represented in this case by parallel tubes that can capture the macroscopic transport properties (Figure 6). The characteristic size of the tubes is determined from mercury intrusion capillary pressure data using Young-Laplace relation, resulting in a relationship between the capillary pressure curve and the permeability of a porous medium. However this model does not represent the rock given that it ignores the pore connectivity (Purcell, 1949).

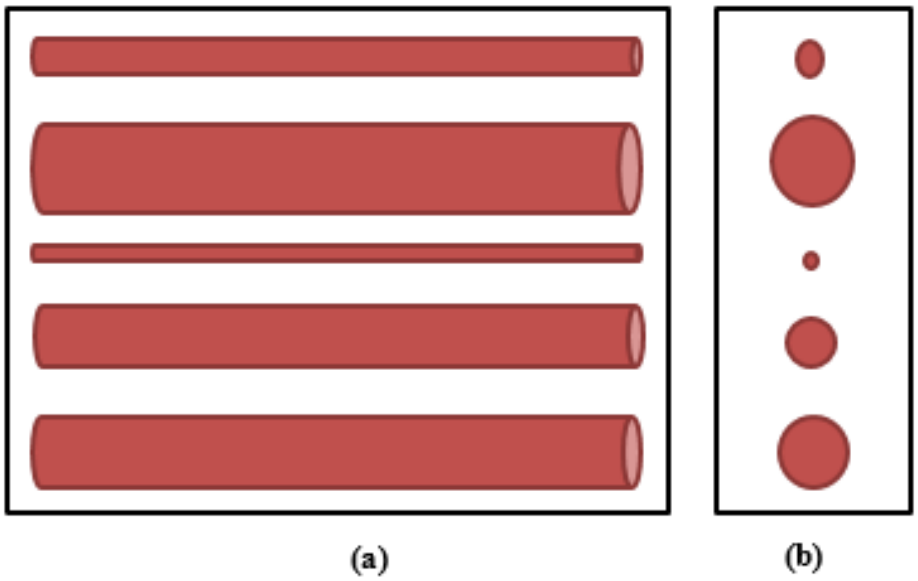

Figure 6. Bundle-of-tubes model used to simplify the pore structure of the rock. The tubes represent the void space. (a) plan view shows length of the tubes, (b) side view shows the radius of the pores that represent the void space.

2.6.1.2. Regular lattice

Fatt (1956), proposed a model that includes the pore connectivity that Purcell's model lacks (Figure 7). It consists of a regular two-dimensional network of tubes of randomly distributed radii that represent the pore sizes. Capillary pressure curves can be derived from the network model and the pore size distributions calculated from these curves.

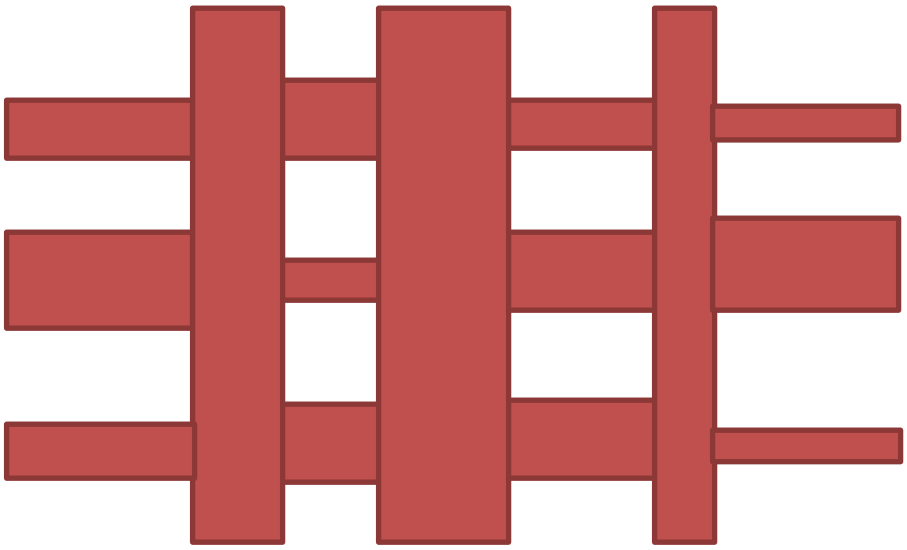

Figure 7. Two-dimensional network of tubes (regular lattice) proposed by Fatt in 1956.

2.6.1.3. Sphere packing

The sphere-packing model assumes that spheres can represent the grains of a sedimentary rock, and the empty spaces between the spheres represent the void space of the porous medium (Figure 8). Using this model, the effects of grain sedimentation, compaction, and diagenesis on transport properties can be analyzed (Bryant, King, & Mellor, 1993; Narváez & Toledo, 2012).

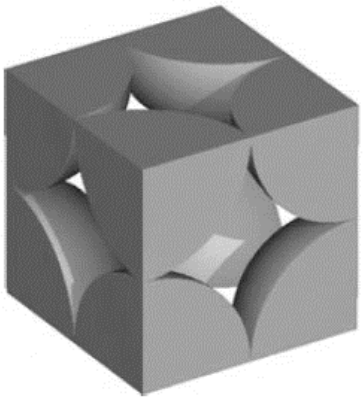

(a)

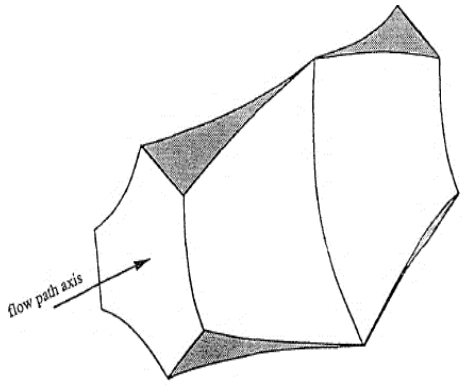

(b)

Figure 8. Sphere packing model (a) example of a simple cubic close packing of uniform spheres that represent the grains (Narváez & Toledo, 2012), (b) Void space between two cells in the sphere packing that represents the flow path or pore space (Bryant, King, et al., 1993).

2.6.1.4. Acyclic pore models

The acyclic pore models main characteristic is that there is a unique path between two points in the model. There are three models included in this category: the bundle-of-tubes model, the tree-like model, and the semi-tree model. In the bundle-of-tubes model, the pore-throat has a uniform size and there is no interconnectivity between different pore-throats as shown in Figure 9. The tree-like model (where the pore-throats distribution

resembles a tree), each pore-throat is accessible through a wider pore-throat (no accessibility restrictions) as shown in Figure 9a. The final model is the semi-tree model (Figure 9b), which is similar to the tree-like model in terms of accessibility, however it differs from the three model because all the sizes that exist between the two throats sizes do not have to be accounted for in the connecting path (Sakhaee-Pour & Bryant, 2015).

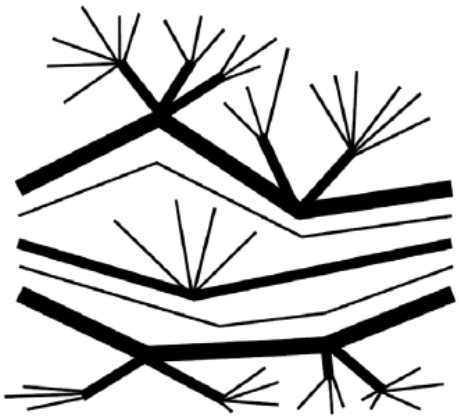

(a)

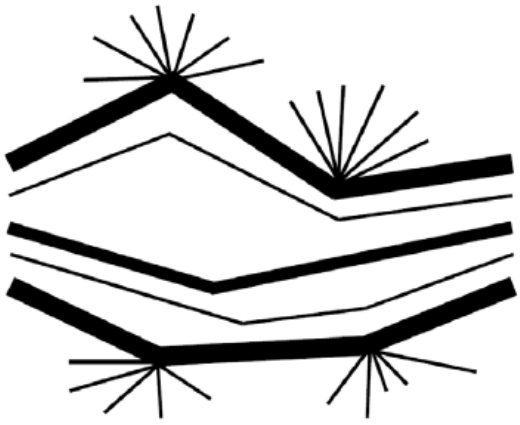

(b)

Figure 9. Acyclic pore models (a) tree-like model and (b) semi-tree model. Narrower throats do not limit the access to the wider throats. From: (Sakhaee-Pour & Bryant, 2015).

Chapter 3: Methodology

3.1. Characteristic behavior of a single conduit in adsorption-desorption

To determine the amount of gas adsorbed in a single conduit as a function of pressure we divide the adsorption process into two stages. First we analyze the thickening of the adsorbed layer that occurs from relative low pressures, and includes the formation of the monolayer at low pressures and multilayer as the pressure increases. Then, we determine the effect of capillary condensation in the single conduit. Finally, we model the desorption process including both evaporation and reduction of the adsorbed layer as the relative pressure is reduced.

The thickness of the adsorbed layer can be determined empirically from experimental curves (t-curves) as mentioned in Chapter 2. The most commonly used equation in the literature is the Halsey's equation (Equation (**6**) developed for nitrogen adsorption isotherms. We use the Halsey's model to determine the thickness of the adsorbed layer on the pore wall of a single conduit. The Halsey's model relates the thickness of the adsorbed layer to the relative pressure as follows (Halsey, 1948):

$$t = 3.54\left(\frac{-5}{ln\left(\frac{P}{P_o}\right)}\right)^{1/3} \tag{6}$$

where t is the thickness of the adsorbed layer in Angstroms, P is the gas pressure, and P_o is the saturation pressure.

Halsey's model is appropriate to determine the amount of gas in the adsorbed layer at small relative pressures (P/P_o). At high relative pressures, Halsey's model is not accurate because it does not account for the condensation and evaporation inside the pore that occurs during adsorption and desorption, respectively. The injected gas changes to liquid and fills the capillarity at relative pressures that are lesser than the bulk saturation pressure of the fluid.

To represent the capillary condensation inside the single conduit we use the Kelvin-Cohan equations derived for both adsorption/condensation and desorption/evaporation as shown in Equations (7) and (8) respectively. (Cohan, 1938)

$$RTln\left(\frac{P}{P_o}\right) = \frac{-\gamma\, V_{mol}}{r_p - t} \tag{7}$$

$$RTln\left(\frac{P}{P_o}\right) = \frac{-2\gamma\, V_{mol}}{r_p - t} \tag{8}$$

where R is the gas constant, T is the temperature, γ is the surface tension, V_{mol} is the molar volume of the liquid phase, $(P/P_o)_{\,adsorption}$ is the relative pressure corresponding to condensation, $(P/P_o)_{\,desorption}$ is the relative pressure corresponding to evaporation, θ is the contact angle, and r_p is the pore radius. Table 2 lists the pertinent parameters for these equations when the fluid used is nitrogen.

Table 2. Input parameters to calculate the relative condensation and evaporation pressures for nitrogen based on Kelvin-Cohan's model (Equations 6 and 7). (Roque-Malherbe, 2007)

R	V_{mol}	γ	θ
$8.314\ \left(\frac{\text{J}}{\text{kmol}}\right)$	$3.467\text{x}10^{-5}\ \left(\frac{\text{m}^3}{\text{mol}}\right)$	$8.85\text{x}10^{-3}\ \left(\frac{\text{N}}{\text{m}}\right)$	0 (°)

Notice from Equation (6) that the thickness of the adsorbed layer on the pore wall is a function of relative pressure. While, the relative pressures relevant to condensation and evaporation are dependent on the original conduit size (Equations. (**7)**and (**8)**). Thus, the conduit size dictates the relative pressures at which capillary condensation occurs.

To calculate condensation and evaporation pressures (Equations. (**7)**and (**8)**), we first suppose that the adsorbed layer thickness is negligible ($t = 0$). We then calculate the thickness for the estimated pressures (Equation (**6)**). Subsequently, we calculate the pressures using the updated thickness and repeat this process to reach convergence. Figure 10 presents the results.

The condensation relative pressure can be determined from Figure 10. In adsorption, there is a sharp increase in relative adsorbed volume at the condensation relative pressure. For instance, the condensation relative pressure is almost equal to 0.55 and 0.87 when the pore size is equal to 3 nm and 20 nm, respectively. There is also a sharp decrease in the adsorbed volume at the evaporation relative pressure during desorption. We suppose that the conduit is filled with liquid when the relative pressure is higher than the condensation relative pressure.

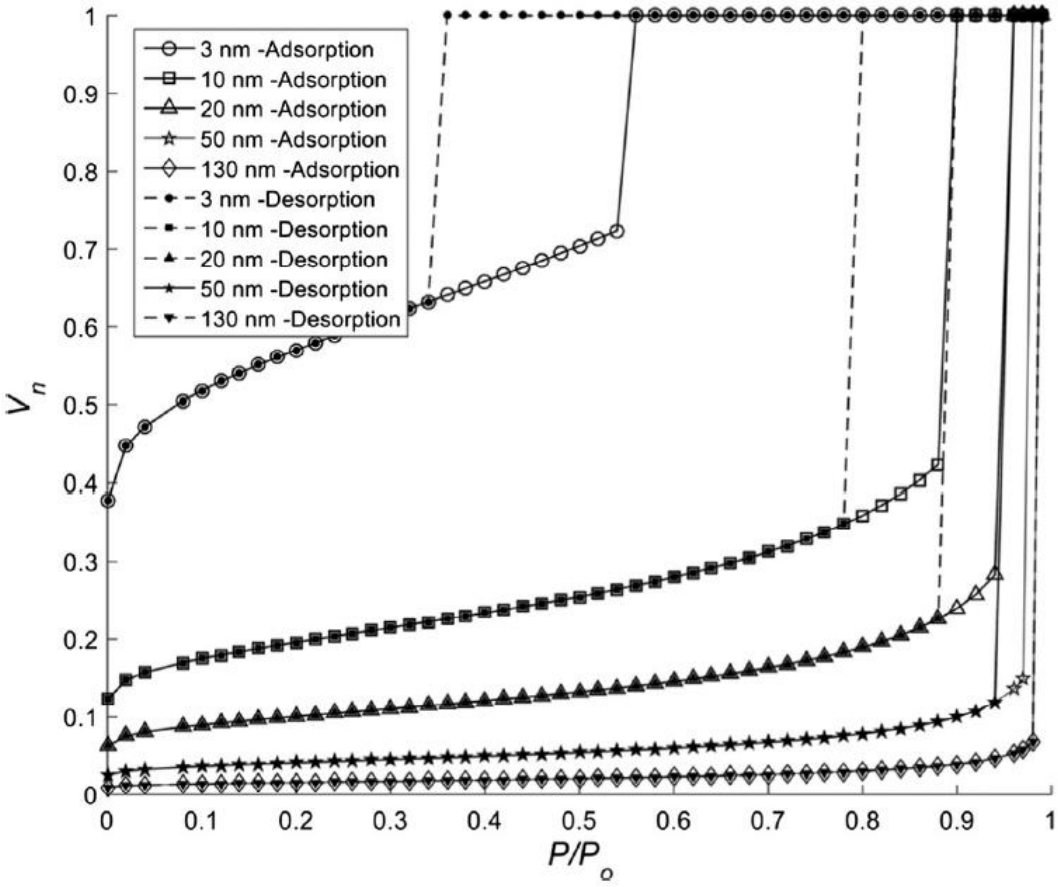

Figure 10. Variation of the normalized adsorbed volume (Vn) with relative pressure (P/Po) depends on the pore-body size of the conduit. The normalized volume is for a single circular tube with different diameters (3 nm, 10 nm, 20 nm, 50 nm, and 130 nm).

We analyze the normalized adsorbed volume (V_n) for a conduit whose pore-body size is smaller than or equal to 130 nm, which is typical for shales. The normalized adsorbed volume is larger for smaller conduits at a given relative pressure (P/P_o). The relative pressure determines the thickness of the adsorbed volume that has a larger volume fraction for narrower conduits.

The difference between condensation and evaporation pressures decreases with the conduit size, which shrinks the hysteresis loop (Compare the results for 3-nm and 130-nm conduits). Thus, the difference between adsorption and desorption curves of single a conduit is more significant for narrower conduits.

3.2. Adsorption-desorption measurements

We use adsorption–desorption isotherms of shales available in the literature (Jiang, Bryant, & Daigle, 2015; Kuila & Prasad, 2013). Table 3 lists the pertinent data about the samples. Nitrogen is used as the adsorbate for the isotherm measurements. The experimental isotherms for the shale samples used in this study are shown in Figure 11(a) and (b). We normalize the measured adsorbed volumes (Vexp-n) to analyze the characteristic behavior with relative pressure (Figure 12).

Table 3. Origin and depth of the shale samples analyzed in this study. Jiang et al. conducted the nitrogen adsorption-desorption measurements for samples 1-2 and Kuila and Passad did for sample 3-4.

	Sample 1	Sample 2	Sample 3	Sample 4
Origin	Barnett Shale	Barnett Shale	Wyoming Montmorillonite (Swy-2)	Georgia Kaolinite (KGa-1b)
Depth	7610 – 7756 ft	7610 – 7756 ft	NA	NA

The hysteresis loop in Figure 12 suggests the presence of mesopores based on our analysis of a single conduit where condensation and evaporation pressures differ significantly from the bulk saturation pressure. The closure relative pressure is almost equal to 0.45

for all samples and there is no significant difference between the adsorbed volumes determined from adsorption and desorption at relative pressures smaller than this value.

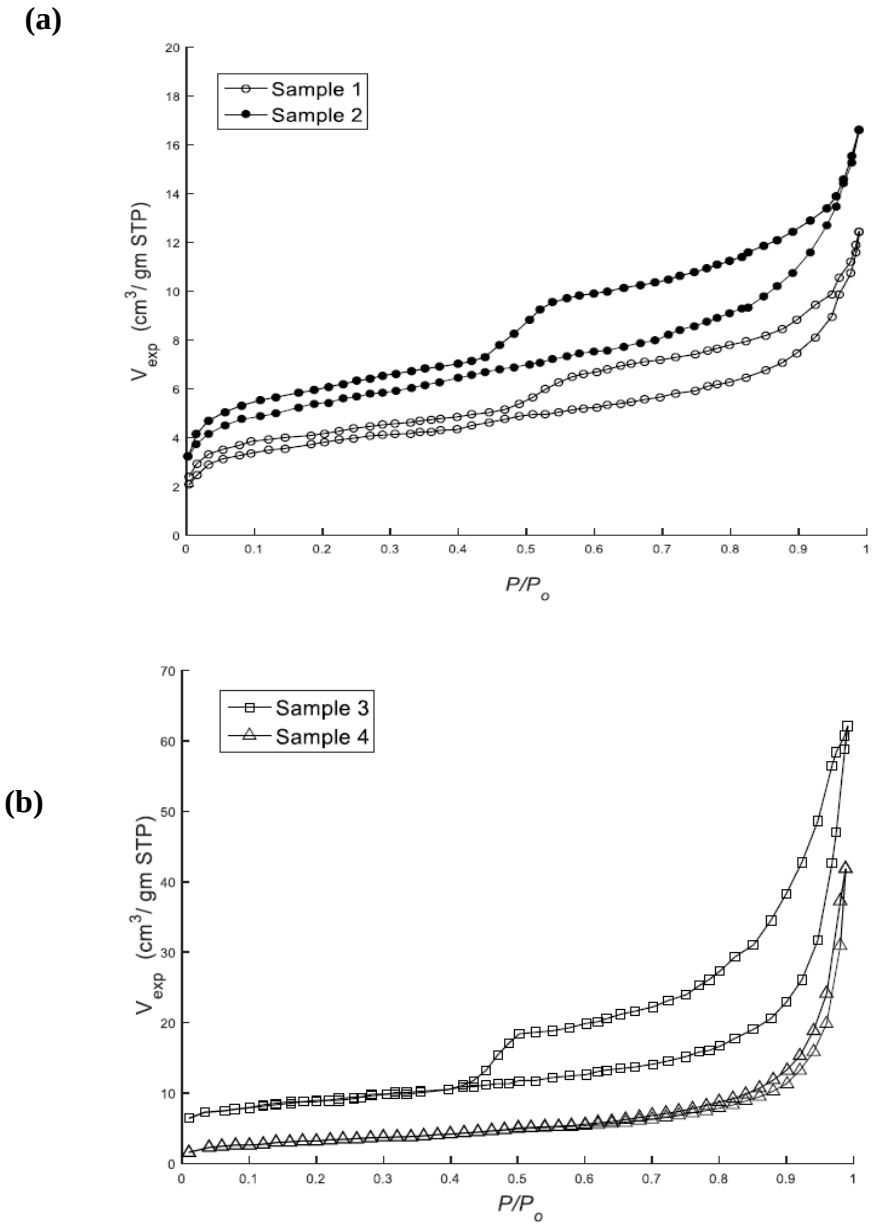

Figure 11. Nitrogen adsorption–desorption isotherms for (a) samples 1 and 2, and (b) samples 3 and 4. (Jiang et al., 2015; Kuila & Prasad, 2013)

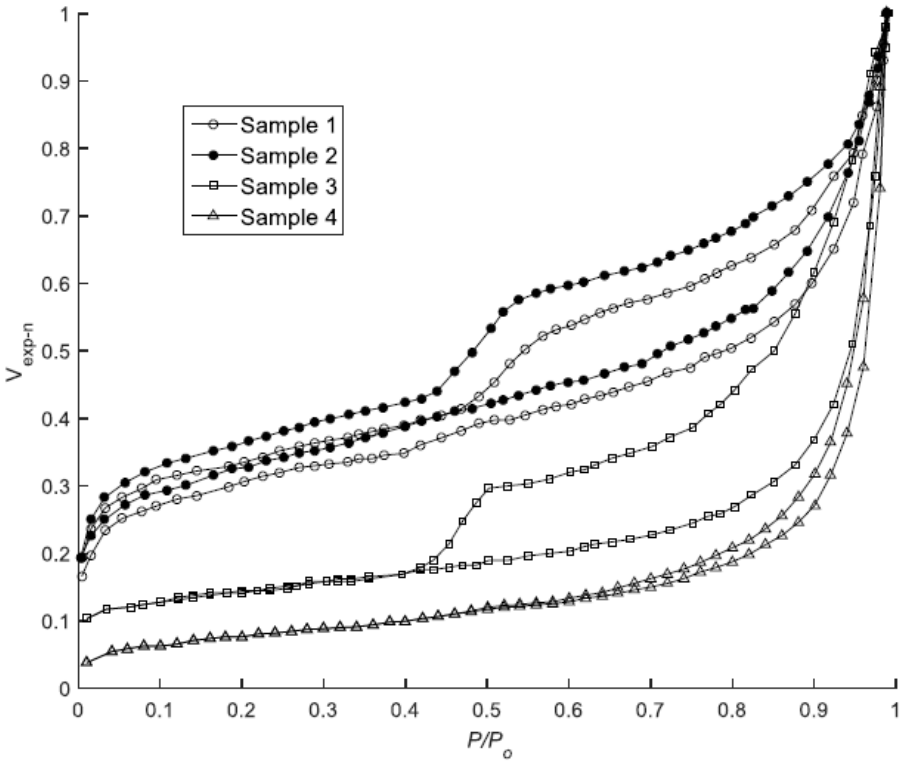

Figure 12. Normalize adsorbed volumes for samples 1 to 4. Different trends with respect to relative pressure can be appreciated for different samples. Sample 4 has the minimum hysteresis which suggests that its pore sizes are larger.

We also use the mercury intrusion capillary pressures for samples 1 and 2 (available from literature) as shown in Figure 13. The linear increase of the capillary pressure with the decreasing wetting phase saturation reveals the absence of a plateau-like trend during drainage. This indicates that the acyclic pore model is representative of the pore space. We do not include the mercury intrusion capillary pressures for samples 3 and 4 because the measurements are documented only for samples 1 and 2, whereas nitrogen adsorption and desorption are reported for all the samples.

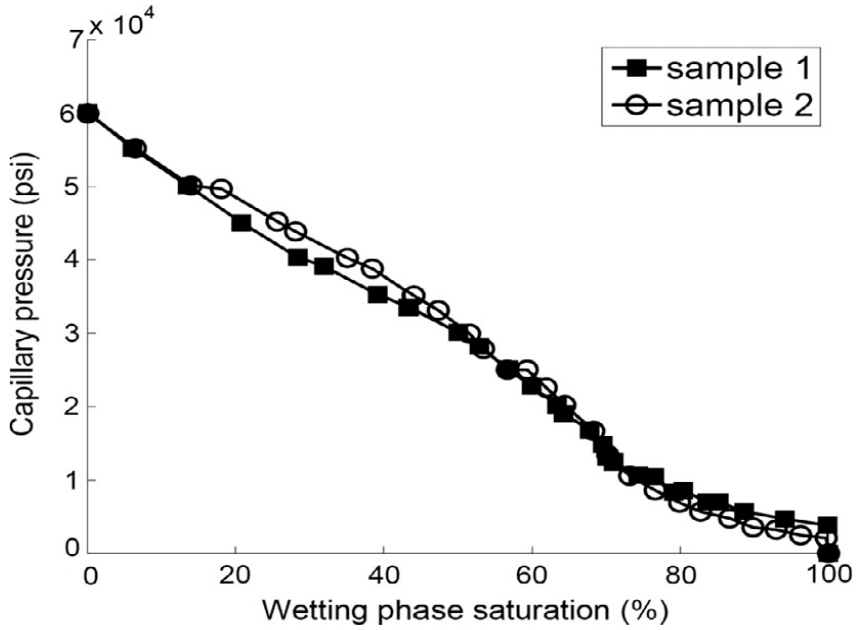

Figure 13. Mercury intrusion capillary pressures of samples 1 and 2, used for determining pore-throat size distribution, shows a non-plateau-like trend and can be captured using the acyclic pore model

3.3. Acyclic pore model

Our study is based on the acyclic pore model (Sakhaee-Pour & Bryant, 2015) to characterize the pore space. There is a unique path between any two points in the model as shown in Figure 14(a), when they are connected (Bethe, 1935). The main feature of the acyclic pore model is that the accessibility of wider pores is not restricted by narrower pores. Narrower pores are accessible from wider throats.

Sakhaee-Pour and Bryant (2015) showed that the acyclic pore model can capture the drainage experiment when the variation of the capillary pressure with wetting phase saturation exhibits a non-plateau-like trend as in Figure 14(b). The model allows us to determine the pore-throat size distribution from the capillary pressure measures shown in Figure 13.

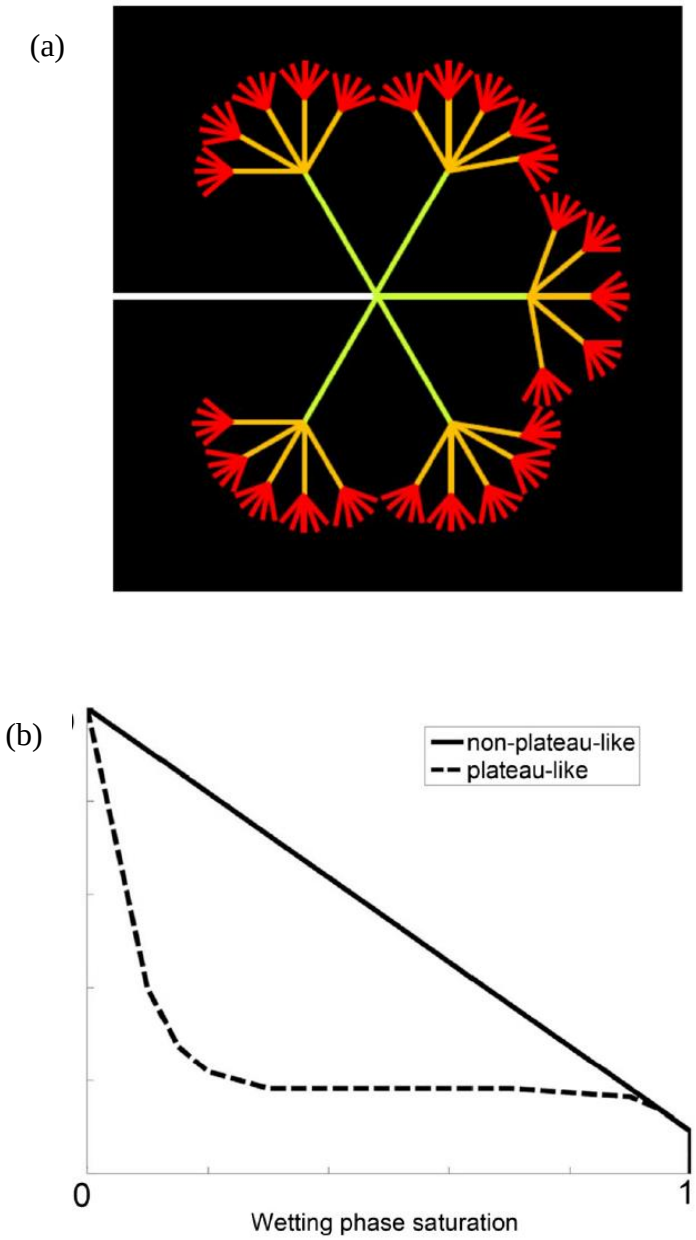

Figure 14. Acyclic pore model. (a) There is a single path between any two points in the model (Bethe, 1935). Red represents the smallest size and white represents the largest size. Narrower pores do not limit access to wider pores (Sakhaee-Pour & Li, 2016) (b) The model can capture the non-plateau-like trend of capillary pressure (Sakhaee-Pour, 2016; Sakhaee-Pour & Bryant, 2015).

We will implement in our study, the fundamental assumption that the accessibility of the wider pores is not limited by narrower pores i.e. acyclic pore model. This will allow us to characterize the pore space not only based on mercury intrusion but also on nitrogen adsorption and desorption neglecting the any accessibility restrictions to the conduits.

3.4. Modeling adsorption-desorption using acyclic pore model

Condensation takes places at higher relative pressure (P/P_o) for wider conduits. The dependency is apparent in Figure 10 where the sudden increase in the adsorbed volume shifts to a higher relative pressure for wider pores. The same holds true for evaporation during desorption. We would have to account for restrictions imposed by narrower pores if they controlled the accessibility of wider pores. Narrower pores do not limit the accessibility of wider pores in the acyclic pore model (Figure 14a). Therefore, we can take into account condensation and evaporation in pores with different pore-body sizes independently in the acyclic model.

We can determine the normalized adsorbed volume as follows:

$$V_n(\frac{P}{P_o}) \propto \sum_{i}^{m} L_i V_{n-i}(\frac{P}{P_o}) \tag{9}$$

where V_n is the normalized adsorbed volume of the porous medium, m is the number of the pore-body size considered, L_i is the normalized length of the conduit size, and V_{n-i} is the specific adsorbed volume of the conduit.

The normalized lengths have to be non-negative to be physically plausible. We can interpret the normalized lengths as weights that relate the characteristic behavior of different conduit sizes to that of the porous medium which imposes the following restrictions:

$$0 \leq L_i \leq 1 \qquad \text{for } i = 1 \text{ to } m \tag{10a}$$

$$\sum_{i}^{m} L_i = 1 \tag{10b}$$

To model adsorption-desorption using acyclic pore model, we need to determine the normalized adsorbed and desorbed volume with relative pressure (P/P_o) for each conduit size. First we determine the specific adsorbed and desorbed volume by extending the application of Equations (6), (7), and (8) for a single conduit, to the total number of conduits relevant for the study. The amount of gas adsorbed or desorbed at his stage is represented as cross-sectional areas adsorbed in the different tubes.

Next, we then determine the normalized length corresponding to each size by minimizing the error through iteration for normalized adsorbed volume V_n calculated from Equation (9) compared with the normalized experimental volume adsorbed V_{exp-n}. We set the error equal to the difference between the measured and modeled volumes as follows:

$$Error = \left| V_{exp-n} - V_n \right| \tag{11}$$

In each iteration, we change the lengths and evaluate their effects on the error:

$$L_i^* = linespace(0,1) \qquad \text{for } i = 1 \text{ to } m \tag{12a}$$

$$L_j^* = L_j + \frac{L_i^* - L_i}{m-1} \qquad j = 1 \text{ to } m\,, j \neq i \tag{12b}$$

where L_i and L_j are the old lengths, and L_i^* and L_j^* are the modified lengths. For each size, we pick a length (L_i^*) and the corresponding L_j^* which minimizes the error in each iteration. We use the modified lengths for a new iteration and repeat this process to reach convergence (Figure 15). We initially suppose that the lengths are equal for all the conduit sizes.

The normalized adsorbed volumes are functions of the pore-body size (Figure 10). This dependency permits us to calculate the pore-body size distribution by accounting for the normalized lengths as follows:

$$Volume\ fraction\ (d_{p-i}) = \frac{L_i(d_{p-i}){d_{p-i}}^2}{\sum_i^m L_i(d_p){d_{p-i}}^2} \tag{13}$$

where $L_i(d_{p-i})$ is the normalized conduit length whose pore-body size is denoted by d_{p-i}. The nominator is an estimate for the corresponding pore volume and the denominator is an estimate for the total pore volume.

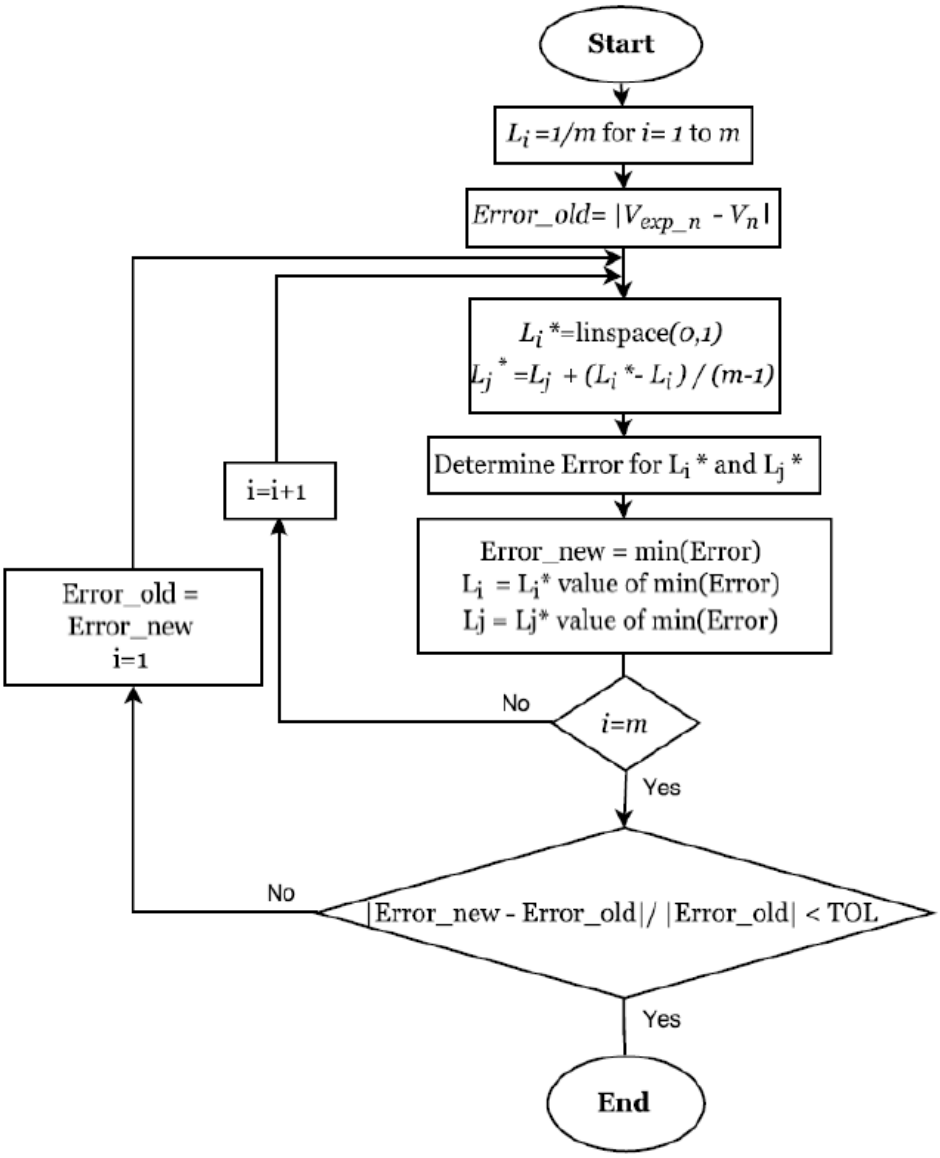

Figure 15. Flowchart for the length iteration implemented in this study based on the acyclic pore model (Zapata & Sakhaee-Pour, 2016).

Chapter 4: Results and Discussion

Our objective was to determine the pore-body size for the four shale samples, as well as the pore-throat. We used nitrogen adsorption-desorption isotherms to characterize the pore-body size distribution (d_p). We also calculated the pore-throat size distribution (d_t) via analyzing mercury intrusion capillary pressure measurements.

4.1. Minimum and maximum pore body sizes

To capture the nitrogen adsorption-desorption that allows us to characterize the pore space of the shale, we have to define the minimum and the maximum pore-body sizes *a priori* to use the acyclic pore model for adsorption-desorption. We take the minimum size equal to 3 nm, which is realistic for shales and valid for the adsorption model (Equation 6). Next, we find the maximum pore-body size by determining the error with the pore-body size.

Figure 16 shows the error variation with the maximum pore-body size for different samples. The minimum error for sample 1 occurs when the maximum pore size is 60 nm; for sample 2 when the maximum pore size is 70 nm; for sample 3 when the maximum pore size is 90 nm; and for sample 4 when the maximum pore size is 110 nm. We will use these pore sizes as the maximum size in each sample to capture the adsorbed volume.

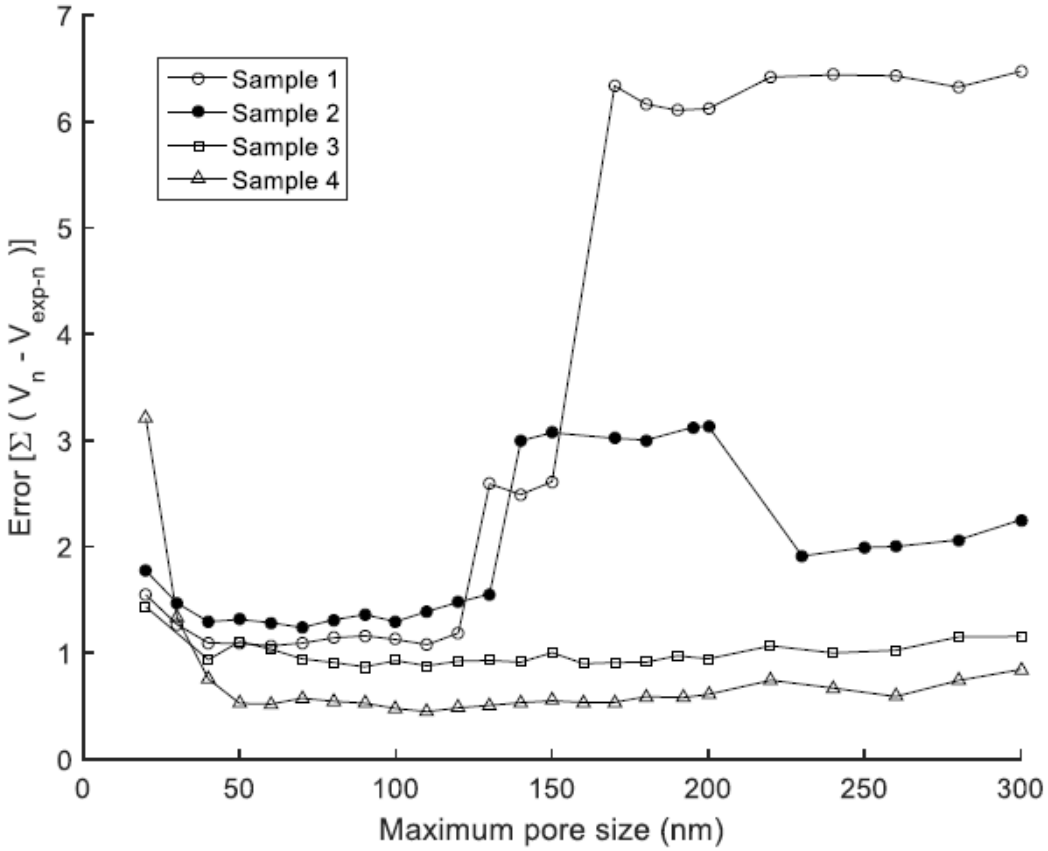

Figure 16. Variation of error with maximum pore-body size for samples 1, 2, 3 and 4. We use the pore-body size corresponding to the minimum error for each sample.

We also tested sensitivity to the number of conduits, by determining the difference between the modeled and the measured volumes adsorbed for different numbers of pore-body sizes. We conclude that using fifty conduit sizes is appropriate because the results do not change significantly with this number of conduits selected. Further, this leads to results with a relatively good resolution.

4.2. Normalized conduits length

We calculated the normalized length of each conduit size (L_i) following the process described in the flowchart in Figure 15. Initially, we suppose the lengths are equal to model the adsorbed and desorbed volume and modify them via iteration. Figure 17, Figure 18, Figure 19, and Figure 20 show the difference between the modeled and the measured volumes for samples 1 to 4.

The difference is plotted for different a different number of iterations for each tube present in the model (each tube represents a different pore size varying from 3nm to the maximum pore size determine for each sample by the minimum error). We stopped the iterations when the results converge. In this case there are no significant changes in the difference show in the y-axis between the results in iterations 15-20.

From Figures 17 to 20 we see how the difference between the modeled and the experimental volumes decreases as the number of iterations increases. The difference plotted in the y-axis for the tube number is higher for lesser conduit sizes (i.e. for lesser tube number) when the number of iterations is low. As the number of iterations increases the difference between the volume measured and modeled reaches the same minimum value for all the conduit sizes.

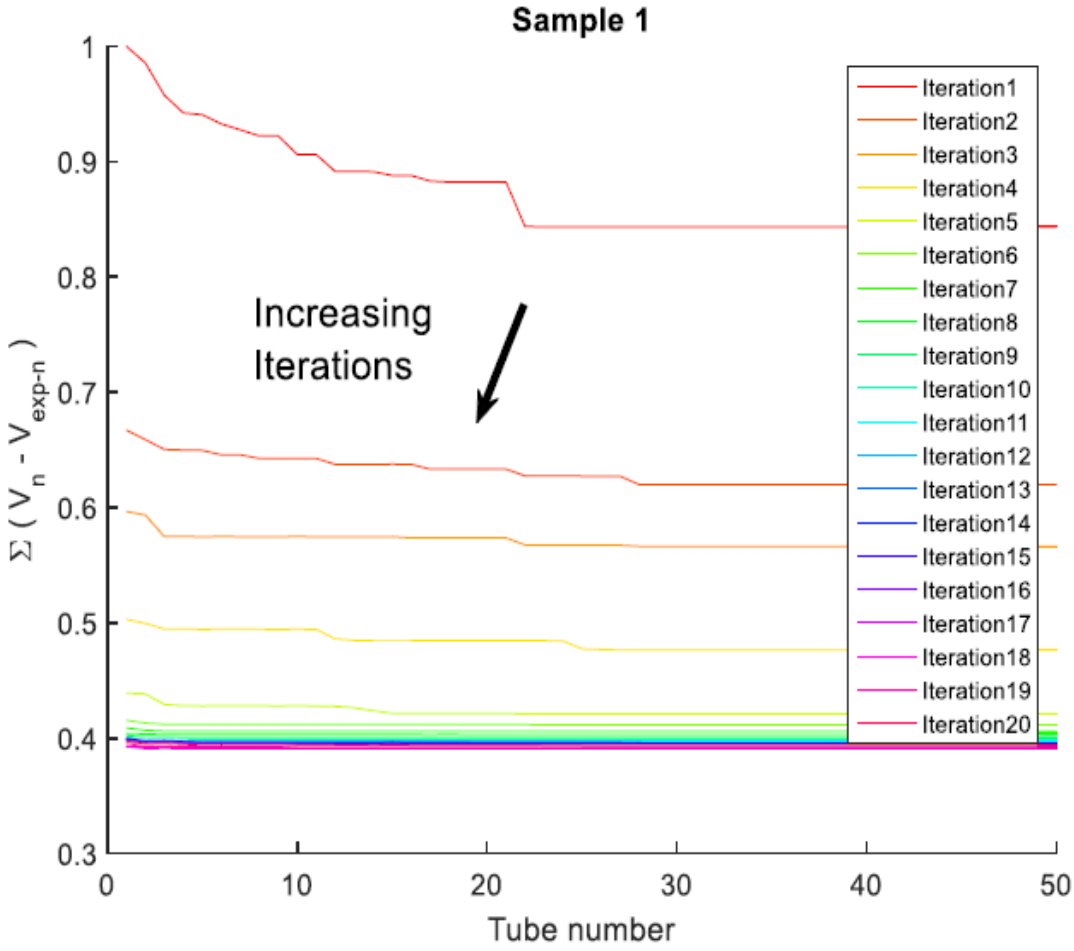

Figure 17. Effect of the number of iterations on the normalized difference between the modeled and measured adsorbed volumes with the tube number for sample 1.

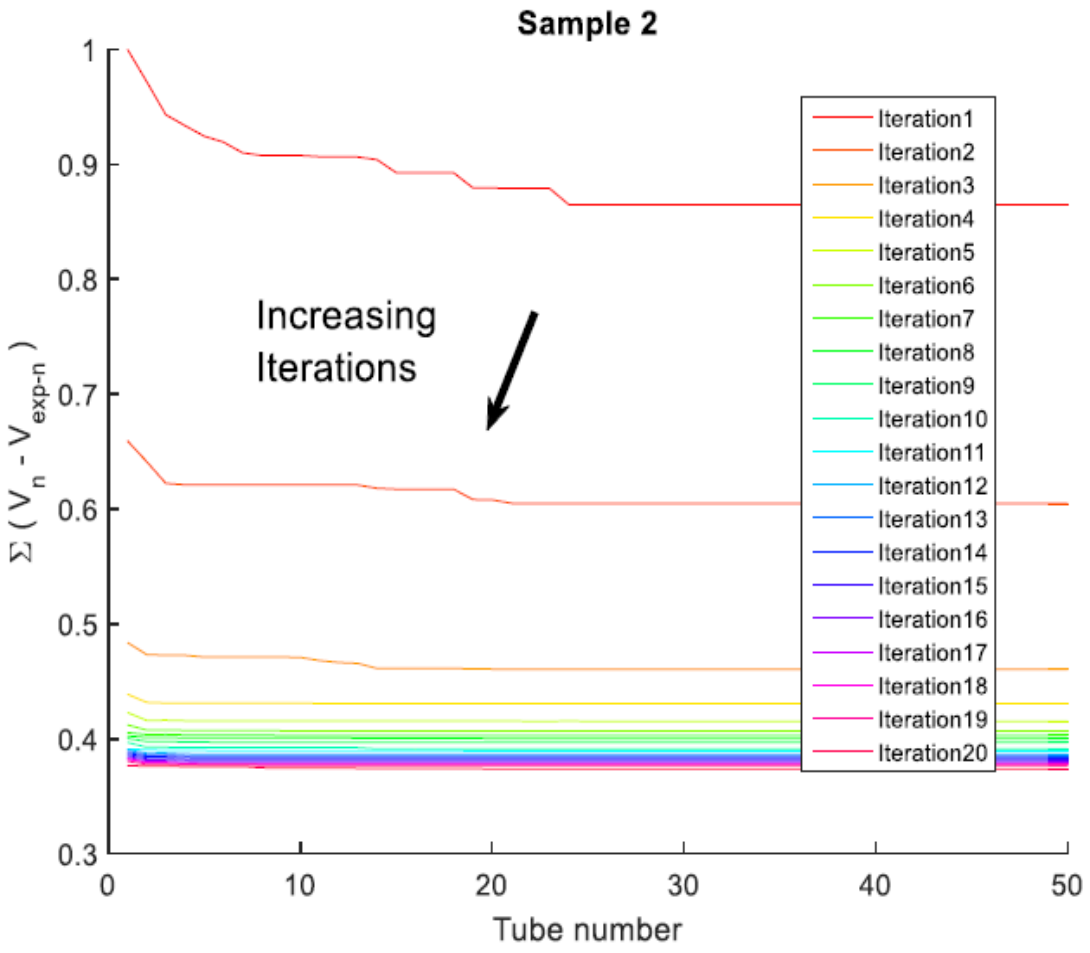

Figure 18. Effect of the number of iterations on the normalized difference between the modeled and measured adsorbed volumes with the tube number for sample 2.

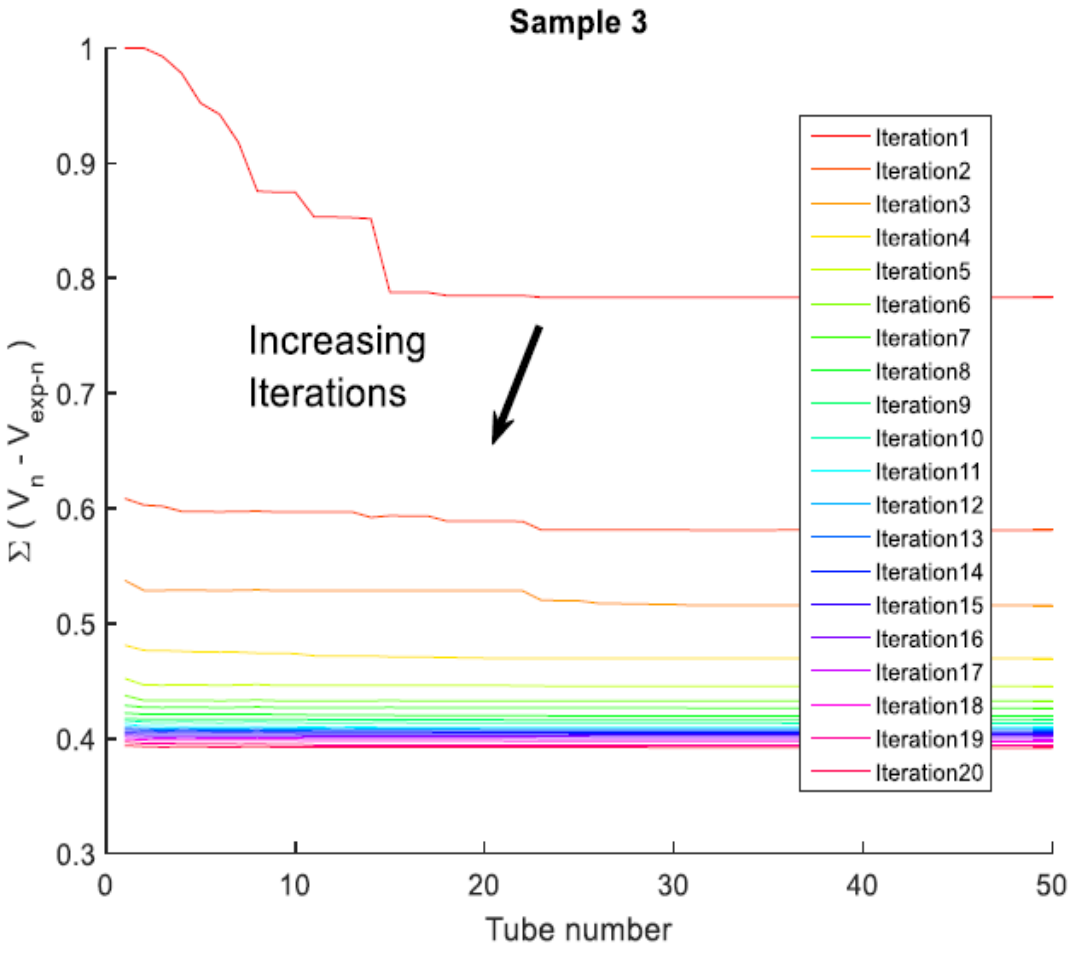

Figure 19. Effect of the number of iterations on the normalized difference between the modeled and measured adsorbed volumes with the tube number for sample 3

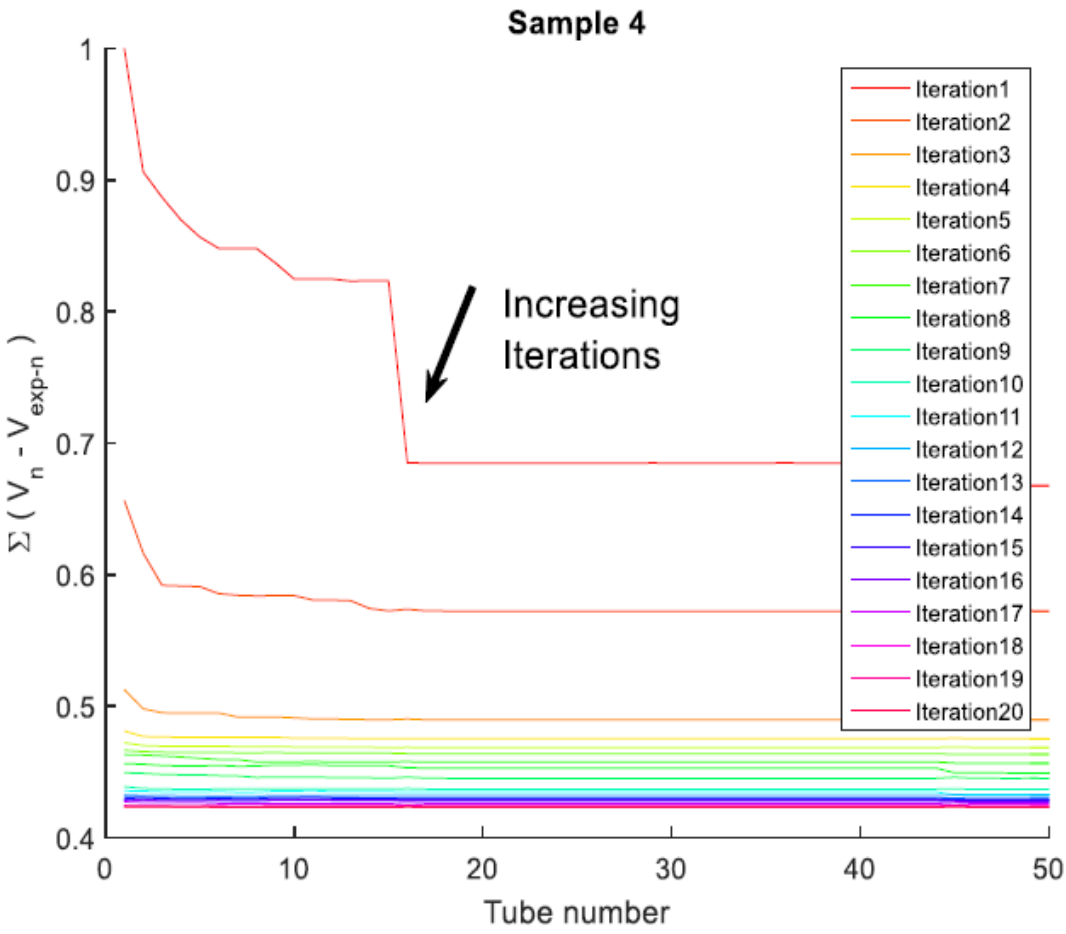

Figure 20. Effect of the number of iterations on the normalized difference between the modeled and measured adsorbed volumes with the tube number for sample 4.

4.3. Adsorption-desorption isotherms

We plot the adsorbed volume captured using the acyclic pore model by accounting for the normalized length and the normalized adsorbed volume. Figure 21, Figure 22, Figure 23, and Figure 24 show the experimental adsorption-desorption curves, the modeled isotherms for the converged iteration (simulation), and the initial guess for samples 1 to 4. The modeled adsorbed volumes, which are the simulation curves (from the iteration process), are improved significantly relative to the initial guess, which is based on equal normalized lengths.

There is a hysteresis in the measured adsorbed volume at low relative pressures in samples 1 and 2 (see Figure 21 and Figure 22) that the model does not capture because it implies a restriction during desorption that the model does not include. The hysteresis for the experimental data points at low pressures for these two samples might be due to the fact that the measurements were conducted too fast for the adsorbed volume to leave. Our model assumes there is no hysteresis at low relative pressures.

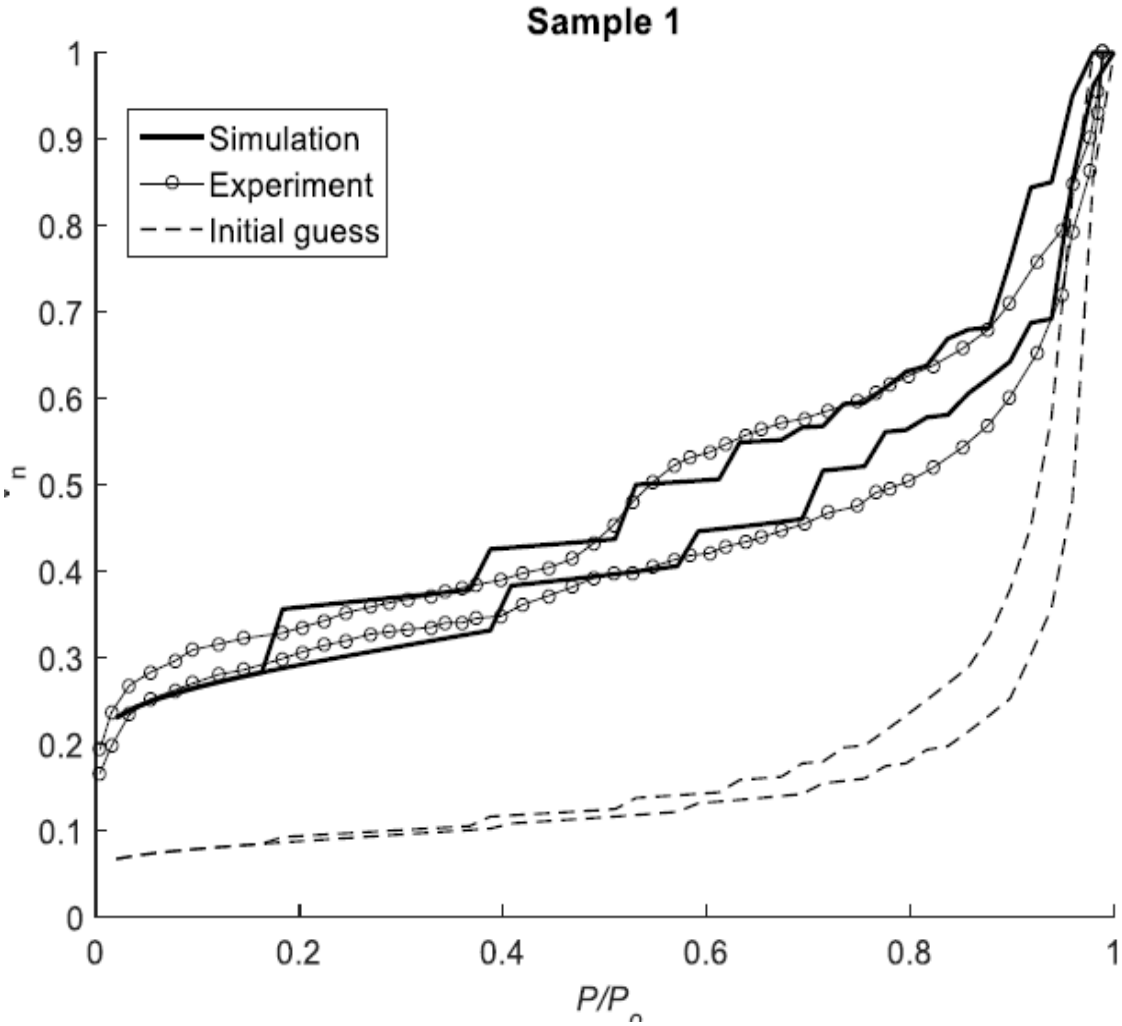

Figure 21. Measured and simulated nitrogen adsorption–desorption isotherms for sample 1.

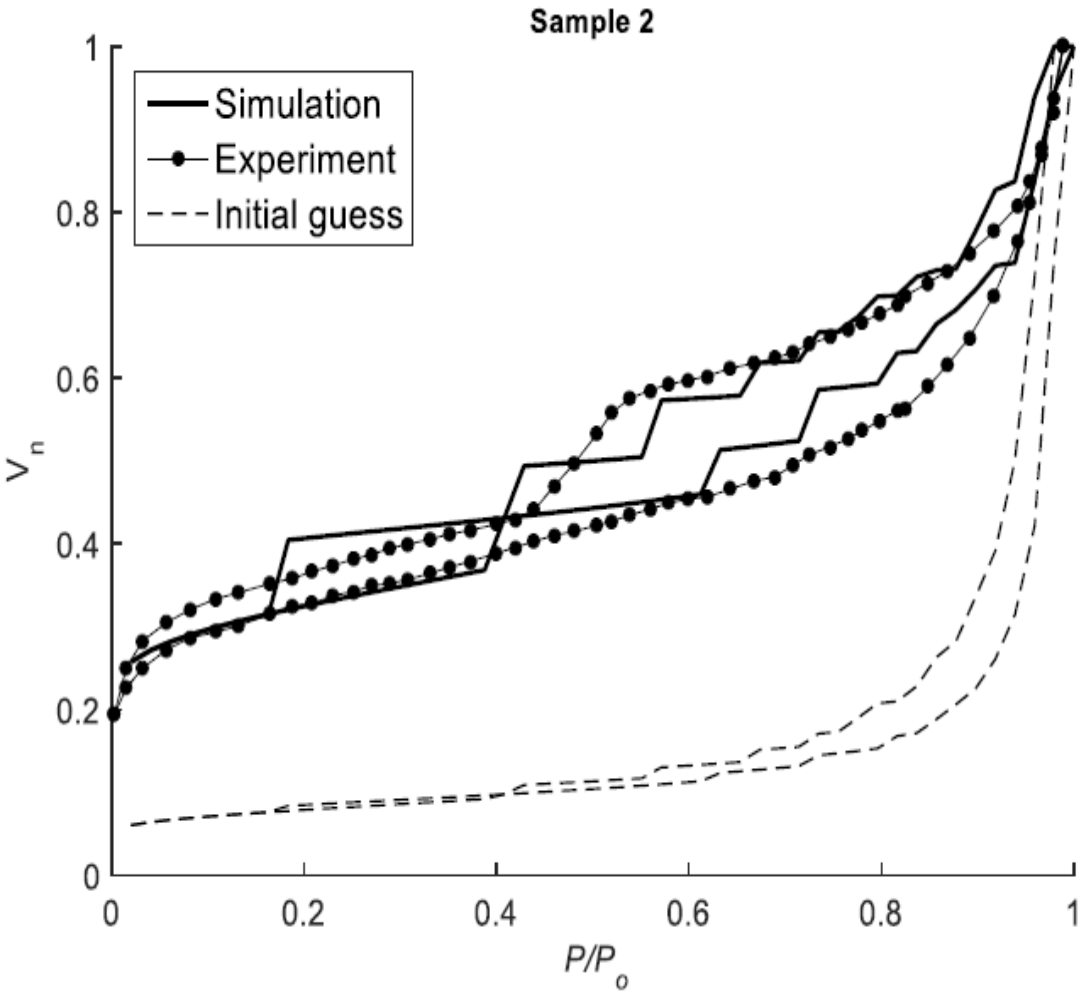

Figure 22. Measured and simulated nitrogen adsorption–desorption isotherms for sample 2.

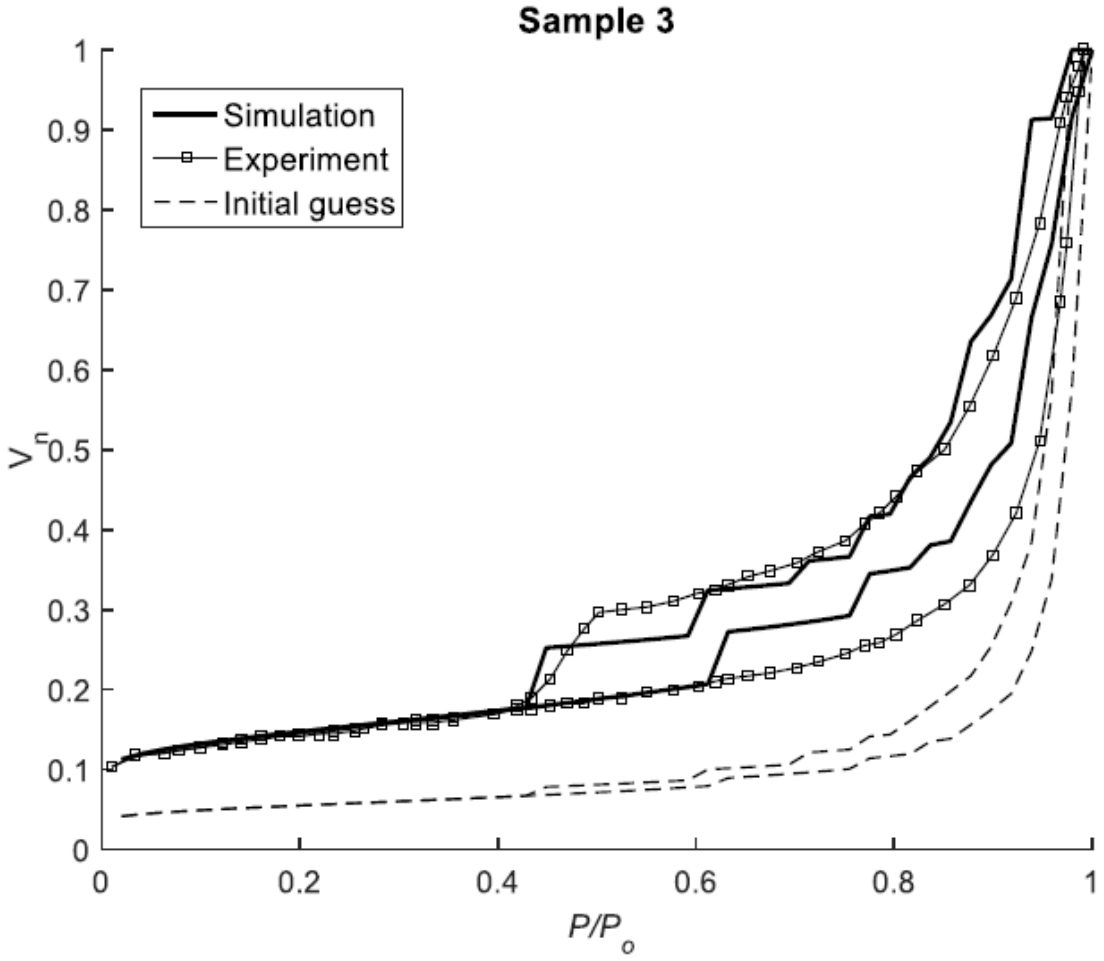

Figure 23. Measured and simulated nitrogen adsorption–desorption isotherms for sample 3.

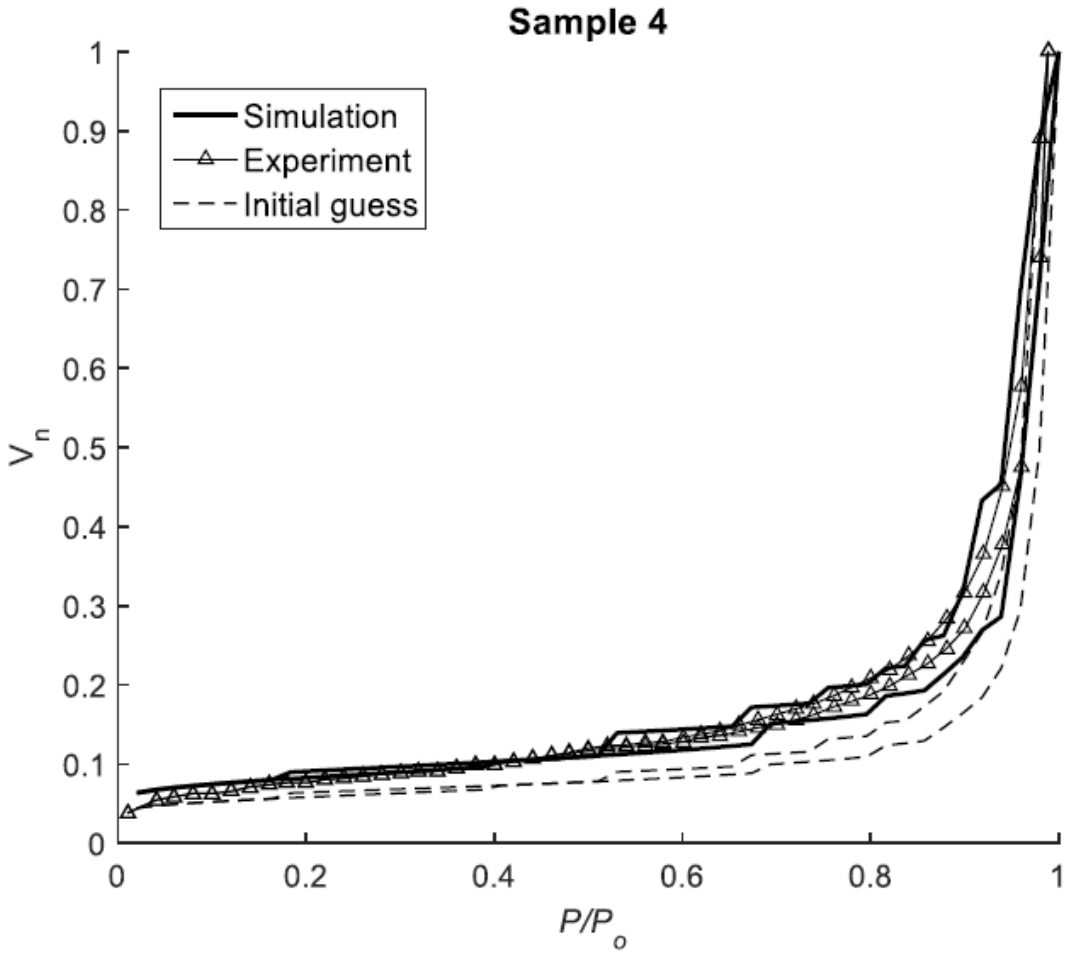

Figure 24. Measured and simulated nitrogen adsorption–desorption isotherms for sample 4.

4.4. Pore-body size distribution

We calculated the pore-body size distributions of samples 1, 2, 3 and 4 using the acyclic pore model and the nitrogen isotherms (Figure 14). We account for the normalized length of each conduit size based on Equation (13).

The pore-body size distribution shows a maximum close to 35 nm for sample 1, for sample 2 the distribution is bimodal with maxima close to 25 and 35 nm as shown in Figure 25. The pore-body size distribution shows a bimodal distribution for Sample 3 with maximum pore-body size close to 30 nm and 80 nm. Sample 4 exhibits a different distribution, whose maximum pore-body size is close to 110 nm as shown in Figure 26.

Figure 27 shows the pore-body size distribution for Barnett shale samples Bar_6 and Bar_2, that are equivalent to samples 1 and 2 in this study. The distributions obtained by Jiang et al. (2015) from nitrogen adsorption isotherms based on the BJH model, exhibit a peak between 10-100 nm in both cases. These distributions agree with the results obtained for samples 1 and 2 from hysteresis of nitrogen adsorption based on the acyclic pore model (see Figure 25).

To compare the results for samples 3 and 4 we use the pore-body size distribution obtained by Kuila & Prasad (2013) for Wyoming Montmorillonite (Sample 3) and Georgia Kaolinite (Sample 4) from nitrogen adsorption isotherms (Figure 28) shows. For sample 3 the distribution exhibits a peak between 60-100 nm while sample 4 around a 100 nm. The distributions obtained based on the acyclic pore model predict the peaks at larger sizes as well (See Figure 26),

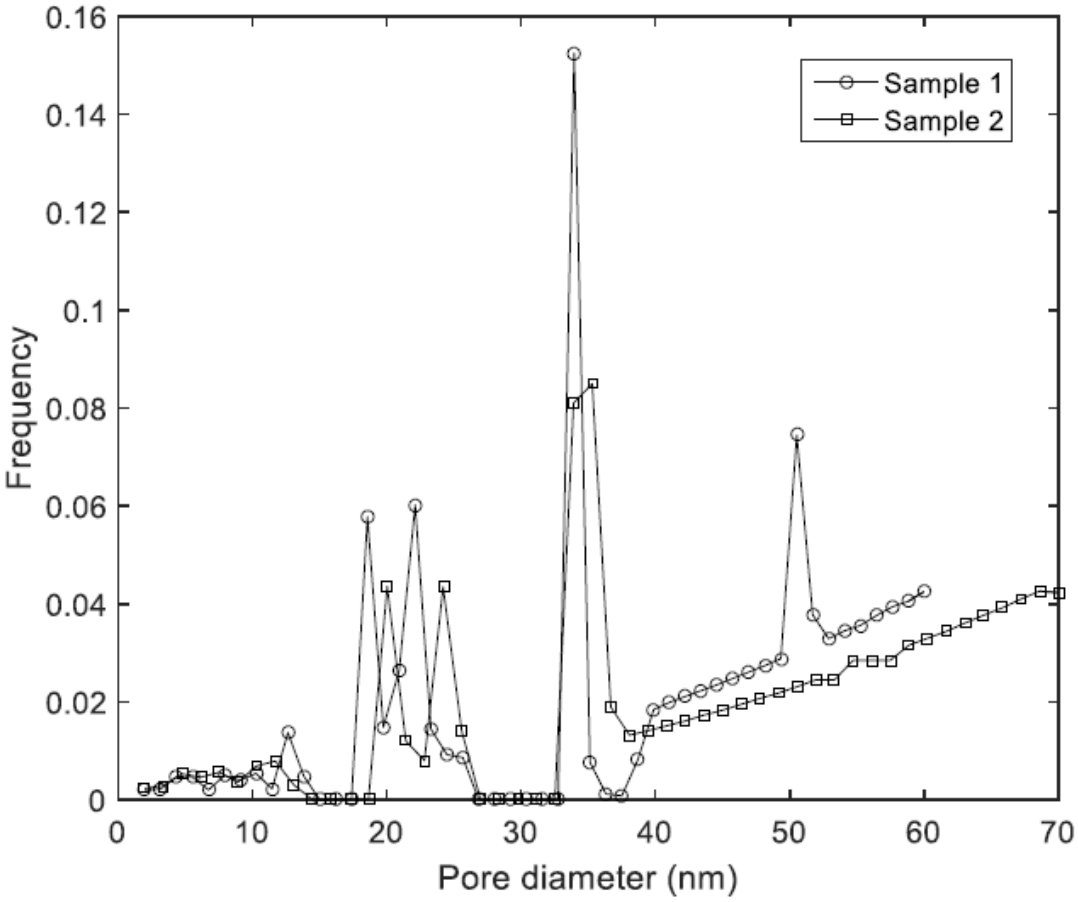

Figure 25. Pore-body size distributions of samples 1 and 2, which are determined by modeling the nitrogen adsorption–desorption measurements. The pore-body size distribution shows a maximum close to 35 nm for sample 1, for sample 2 the distribution is bimodal with maxima close to 25 and 35 nm.

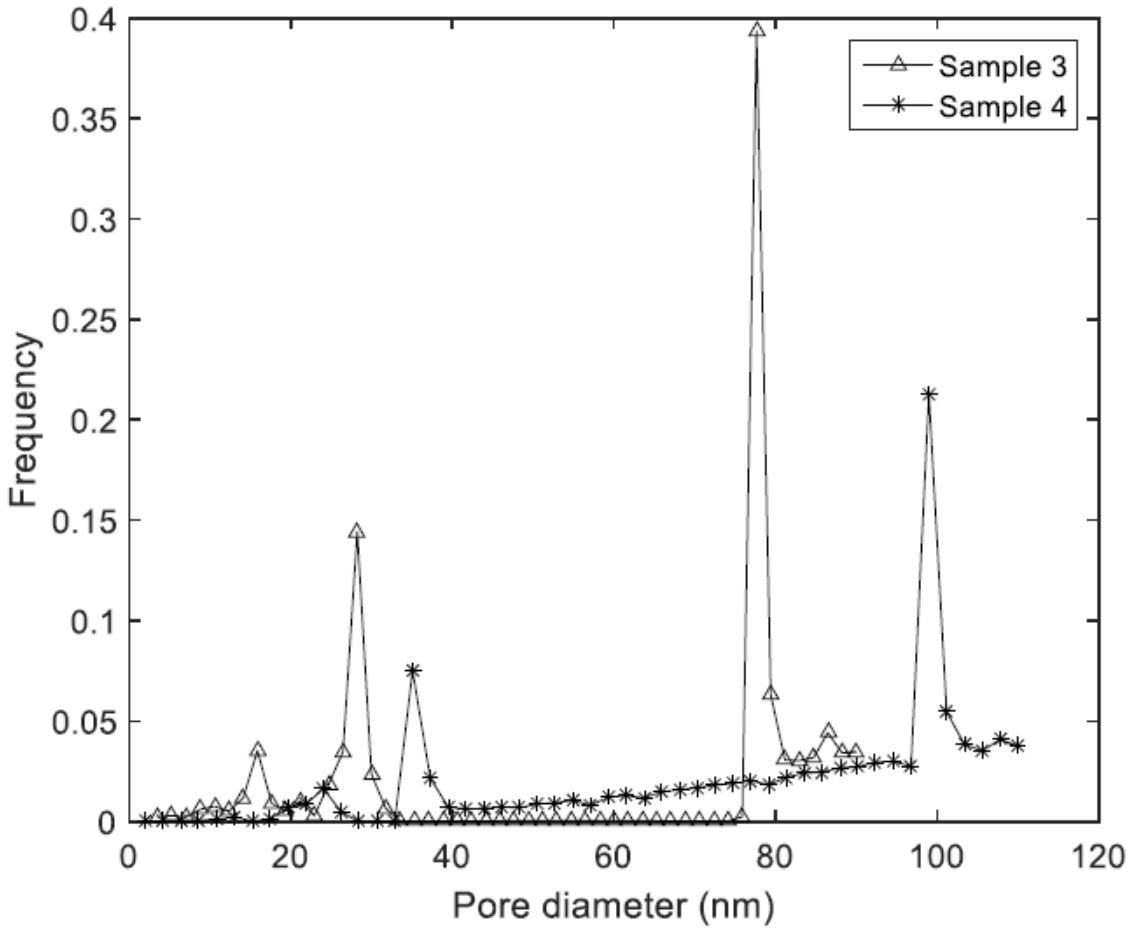

Figure 26. Pore-body size distributions of samples 3 and 4, which are determined by modeling the nitrogen adsorption–desorption measurements. The pore-body size distribution shows a bimodal distribution for Sample 3 with maximum pore-body size close to 30 nm and 80 nm. Sample 4 exhibits a different distribution, whose maximum pore-body size is close to 110 nm

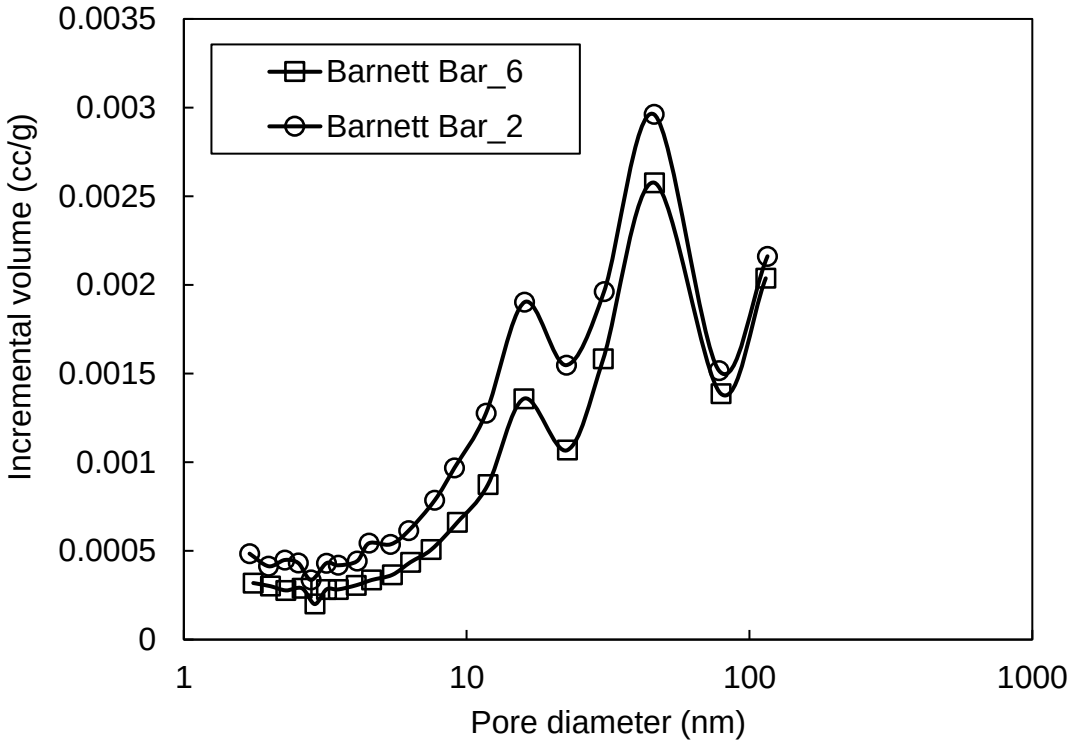

Figure 27. Pore-body size distribution for Barnett shale samples from nitrogen adsorption by Jiang et al. (2015). The pore diameter ranges from 1 nm to 100 nm in both cases, with a peak between 20 and 70 nm. These results agree with the distributions obtained for samples 1 and 2, based on the hysteresis of nitrogen adsorption and the acyclic pore model (Figure 25).

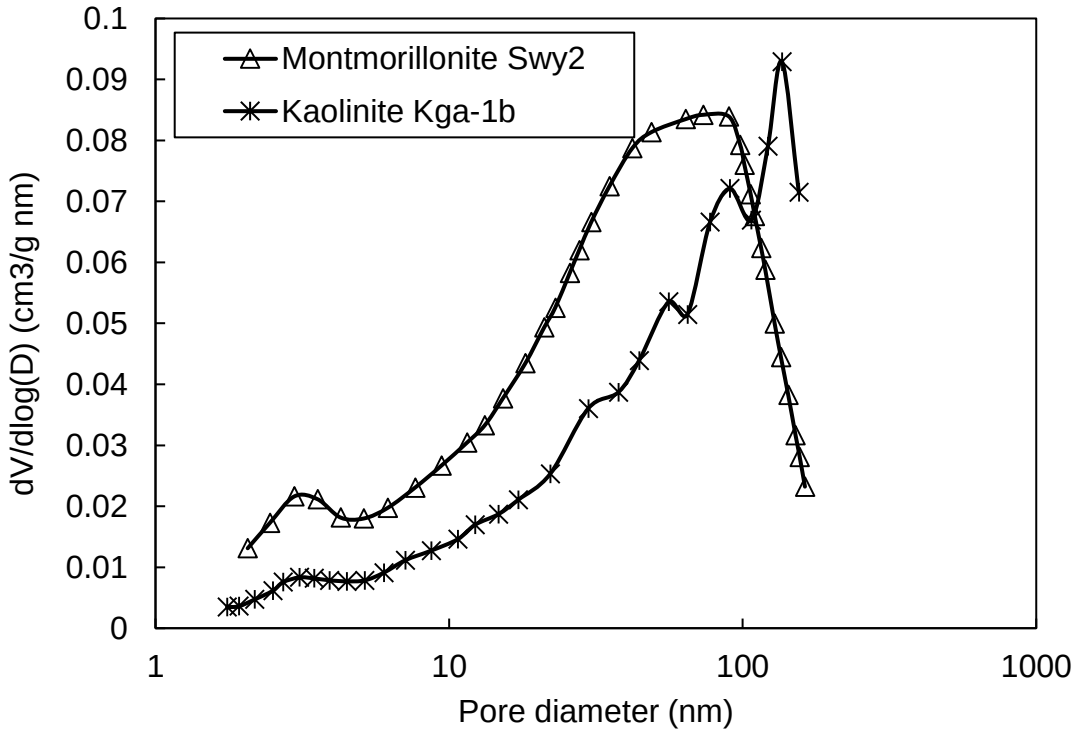

Figure 28. Pore size distribution for Wyoming Montmorillonite (Sample 3) and Georgia Kaolinite (Sample 4) from nitrogen adsorption isotherms obtained by Kuila & Prasad (2015). The Montmorillonite exhibit a peak between 50-100 nm, while the Kaolinite near to 100 nm. The distributions obtained based on the acyclic pore model also predict the peaks at larger pore sizes (Figure 26).

4.5. Pore-body and pore-throat size distributions comparison

We compared pore-body and pore-throat size distributions for samples 1-2 whose relative measurements are available in the literature. The distributions are based on the interpretation of the nitrogen adsorption-desorption and mercury intrusion. Each technique is appropriate for different characteristic sizes of the pore structure, the former is representative of the pore-body and the latter of the pore-throat. The integration of both methods allows us to fully characterize the pore space.

Figure 29 quantifies the difference between the two sizes in a single model (acyclic pore model) for pore space characterization. The volume faction of pore-throat is much larger than that of the pore-body size for smaller sizes. The difference becomes less significant for larger sizes. The large volume fraction observed for larger pore-throat size can be relevant to micro fractures that remain open during the mercury intrusion tests because they were conducted with no confining stress. The pore-throat size is more important for understanding flow conductance, whereas the pore-body size plays a more-important role in determining hydrocarbon storage.

The transport properties change significantly when we go from the macroscale, or even the microscale, to the nanoscale. The relevant changes in hydrocarbon transport properties in shales can be classified into storage, which is controlled mainly by the pore body, and fluid displacement, which is dictated mainly by the pore throat. The pore-body size distributions for samples 1 and 2 are relatively similar, whereas the pore-throat size distributions are different. The similarity suggests that the transport properties controlled

by the characteristic size of the bulk volume, such as density, could be relatively similar for the analyzed samples. This demonstrates that, if other governing parameters are identical, the transport properties controlled by the pore throat size can be different. The difference between the changes in predicted transport properties highlights the importance of distinguishing between pore-throat and pore-body sizes for shales.

We can associate the pore volume of a single pore with its pore throat and pore body sizes. There is no general model for relating the two sizes because of the complicated topology of the pore. The two sizes are different, not only because they specify different topological parameters, but also because they control different transport properties. The lack of a general model reveals the difficulty of relating the volume fractions corresponding to equal pore throat and pore body sizes. Figure 29 reveals that the volume fraction of the pore-body size is smaller than that of the pore-throat size for small sizes, and the difference between the volume fractions becomes less significant as the size increases. Our interpretation is that the transport properties of a significant fraction of the pore volume, whose pore-body sizes have a large volume fraction, are controlled by the small pore throats. Further, the large volume fraction of the small pore-throat size indicates that the corresponding pore volume is significant.

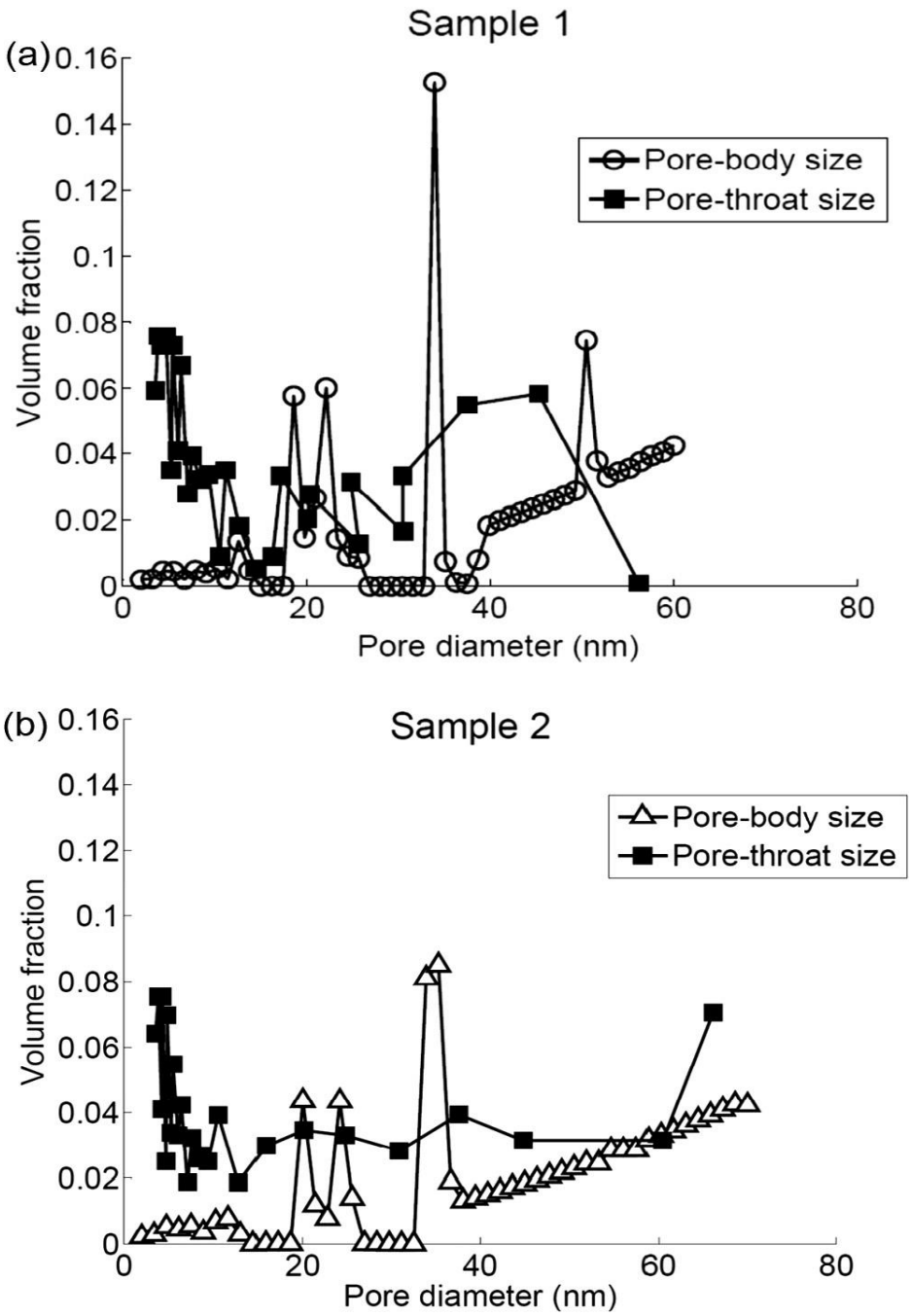

Figure 29. Pore-body and pore-throat size distributions of samples 1 and 2 that are, respectively, based on the interpretation of the nitrogen adsorption–desorption and mercury intrusion. The two sizes allow us to characterize the pore space using the acyclic pore model.

Conclusions

Our objective was to characterize the pore space of a shale formation using nitrogen adsorption-desorption and mercury intrusion. Both are dependent on the pore structure; while the former is more appropriate for characterizing the pore body, the latter is for the pore throat. We used the acyclic pore model, which accounts for the limited connectivity in the connected path of the pore space at the core scale, to characterize the pore space. Our model allowed us to capture sorption hysteresis including different adsorption mechanisms, such as the thickening of the adsorbed layer and the capillary condensation. It also enabled us to capture mercury intrusion capillary pressures. This work contributes to the fundamental understanding of the shale formation by quantifying the difference between the two characteristic sizes. A better understanding of the characteristic sizes is critical for predicting the stored volume, controlled by the pore volume, and its hydraulic conductivity, dictated by the pore throat.

References

Balbuenat, P. B., & Gubbins, K. E. (1993). Theoretical interpretation of adsorption behavior of simple fluids in slit pores. *Langmuir*, *9*(7), 1801–1814. http://doi.org/10.1021/la00031a031

Barrett, E. P., Joyner, L. G., & Halenda, P. P. (1951). The Determination of Pore Volume and Area Distributions in Porous Substances. I. Computations from Nitrogen Isotherms. *Journal of the American Chemical Society*, *73*(1), 373–380. http://doi.org/10.1021/ja01145a126

Bethe, H. A. (1935). Statistical theory of superlattices. *Proc R Soc Lond A*, *150*(552–75).

Boucher, E. A. (1976). Review porous materials: structure, properties and capillary phenomena, *11*, 1734–1750.

Brunauer, S., Deming, L. S., Deming, W. E., & Teller, E. (1940). On a theory of the van der Waals adsorption of gases. *Journal of The American Chemical Society*, *62*(7), 1723–1732. http://doi.org/10.1021/ja01864a025

Brunauer, S., Emmett, P. H., & Teller, E. (1938). Adsorption of Gases in Multimolecular Layers. *Journal of the American Chemical Society*, *60*(1), 309–319. http://doi.org/citeulike-article-id:4074706\rdoi: 10.1021/ja01269a023

Brunauer, S., Mikhail, R. S., & Bodor, E. . (1967). Pore structure analysis without a pore shape model. *Journal of Colloid and Interface Science*, *24*(4), 451–463. http://doi.org/10.1016/0021-9797(67)90243-3

Bryant, S. L., King, P. R., & Mellor, D. W. (1993). Network model evaluation of permeability and spatial correlation in a real random sphere packing. *Transport in Porous Media*, *11*(1), 53–70. http://doi.org/10.1007/BF00614635

Bryant, S. L., Mellor, D. W., & Cade, C. a. (1993). Physically representative network models of transport in porous media. *AIChE Journal*, *39*(3), 387–396. http://doi.org/10.1002/aic.690390303

Cohan, L. H. (1938). Sorption hysteresis and the vapor pressure of concave surfaces. *Journal of the American Chemical Society*, *60*(2), 433–435.

Cranston, R. W., & Inkley, F. A. (1957). The Determination of Pore Structures from Nitrogen Adsorption Isotherms. *Advances in Catalysis, Volume 9*, 143–154. http://doi.org/10.1016/S0360-0564(08)60163-7

De Boer, J. H., Broekhoff, J. C. P., Linsen, B. G., & Meijer, a L. (1967). Studies on pore systems in catalysts VIII. The adsorption of krypton and nitrogen on graphitized carbon. *Journal of Catalysis*, *7*, 135–139. http://doi.org/10.1016/0021-9517(67)90051-6

De Boer, J. H., Lippens, B. C., Linsen, B. G., Broekhoff, J. C. P., van den Heuvel, a., & Osinga, T. J. (1966). The t-curve of multimolecular nitrogen adsorption. *Journal of Colloid and Interface Science*, *21*(4), 405–414. http://doi.org/10.1016/0095-8522(66)90006-7

Donohue, M., & Aranovich, G. (1998). Adsorption hysteresis in porous solids. *Journal of Colloid and Interface Science*, *205*(1), 121–30. http://doi.org/10.1006/jcis.1998.5639

Dubinin, M. M. (1989). Fundamentals of the theory of adsorption in micropores of carbon adsorbents: Characteristics of their adsorption properties and microporous structures. *Carbon*, *27*(3), 457–467. http://doi.org/10.1016/0008-6223(89)90078-X

Everett, D. H., Sing, K. S. W., Haul, R. A. W., Moscou, L., Pierotti, R. A., Roquerol, J., & Siemieniewska, T. (1985). Reporting physisorption data for gas/solid systems — with special reference to the determination of surface area and porosity. *Pure and Applied Chemistry*, *57(4)*, 603–619.

Fatt, I. (1956). The Network Model of Porous Media. *Petroleum Transactions, AIME*, *207*, 144–181.

Frooqnia, A., Torres-Verdín, C., Sepehrnoori, K. and A-Pour, R. 2016a. Transient coupled borehole/formation fluid-flow model for interpretation of oil/water production logs. *SPE Journal*. SPE-183628-PA (in press; posted 21 June 2016). http://dx.doi.org/10.2118/183628-PA.

Frooqnia, A., Torres-Verdín, C., Sepehrnoori, K. and A-Pour, R. 2016b. Inference of rock pressure-production properties from gas-oil production logs. *Journal of Natural Gas Science and Engineering*. In press; posted 13 October 2016. http://dx.doi.org/10.1016/j.jngse.2016.10.018.

Frooqnia, A. 2014. *Numerical simulation and interpretation of borehole fluid-production*

measurements. Ph.D. Dissertation, The University of Texas at Austin, Austin, Texas.

Frooqnia, A., Torres-Verdín, C., A-Pour, R., Sepehrnoori, K., and Mohebbinia, S. 2013. Estimation of near-wellbore relative permeability from numerical simulation and inversion of time-lapse multi-phase production logs. Paper VVV presented at the SPWLA 54th International Logging Symposium, New Orleans, Louisiana, 22-26 June.

Frooqnia, A., A-Pour, R., Torres-Verdín, C., and Sepehrnoori, K. 2011. Numerical simulation and interpretation of production logging measurements using a new coupled wellbore-reservoir model. Paper VV presented at the SPWLA 52nd International Logging Symposium, Colorado Springs, Colorado, 14-18 May.

Graf, K., & Kappl, M. (2003). *Physics and chemistry of interfaces*.

Gubbins, K. E., Long, Y., & Śliwinska-Bartkowiak, M. (2014). Thermodynamics of confined nano-phases. *Journal of Chemical Thermodynamics*, 169–183. http://doi.org/10.1016/j.jct.2014.01.024

Halsey, G. (1948). Physical adsorption on non-uniform surfaces. *The Journal of Chemical Physics*, *16*(10), 931. http://doi.org/10.1063/1.1746689

Jiang, C., Bryant, S., & Daigle, H. (2015). A bundle of short conduits model of the pore structure of gas shale. *Unconventional Resources Technology Conference (URTEC).*, 20–22. http://doi.org/10.15530/urtec-2015-2169349

Jura, G., & Harkins, W. D. (1943). A new adsorption isotherm which is valid over a very wide range of pressure. *The Journal of Chemical Physics*, *11*(9), 430. http://doi.org/10.1063/1.1723870

Kaneko, K. (1994). Determination of pore size and pore size distribution. *Journal of Membrane Science*, *96*(1–2), 59–89. http://doi.org/10.1016/0376-7388(94)00126-X

Kate, J. M., & Gokhale, C. S. (2006). A simple method to estimate complete pore size distribution of rocks. *Engineering Geology*, *84*(1–2), 48–69. http://doi.org/10.1016/j.enggeo.2005.11.009

Kuila, U., & Prasad, M. (2013). Specific surface area and pore-size distribution in clays and shales. *Geophysical Prospecting*. http://doi.org/10.1111/1365-2478.12028

Langmuir, I. (1918). The adsorption of gases on plane surfaces of glass, mica and platinum. *Journal of the American Chemical Society*, *40*(9), 1361–1403. http://doi.org/doi: 10.1021/ja02242a004

Mousavi, M. A., & Bryant, S. L. (2012). Connectivity of Pore Space as a Control on Two-Phase Flow Properties of Tight-Gas Sandstones. *Transport in Porous Media*, *94*(2), 537–554. http://doi.org/10.1007/s11242-012-0017-x

Narváez, A., & Toledo, P. G. (2012). Pore Space Microstructure Evolution of Regular Sphere Packings Undergoing Compaction and Cementation. *Transport in Porous Media*, *95*(1), 71–89. http://doi.org/10.1007/s11242-012-0033-x

Naumov, S. (2009). *Hysteresis Phenomena in Mesoporous Materials*. Leipzig University.

Ovaysi, S., Wheeler, M. F., & Balhoff, M. (2014). Quantifying the Representative Size in Porous Media. *Transport in Porous Media*, *104*(2), 349–362. http://doi.org/10.1007/s11242-014-0338-z

Purcell, W. R. (1949). Capillary Pressures - Their Measurement Using Mercury and the Calculation of Permeability Therefrom. *Journal of Petroleum Technology*, *1*(2), 1949. http://doi.org/10.2118/949039-G

Roque-Malherbe, R. M. A. (2007). *Adsorption and Diffussion in Nanoporous Materials*.

Rouquerol, J., Rouquerol, F., Llewellyn, P., Maurin, G., & Sing, K. S. (2013). *Adsorption by powders and porous solids: principles, methodology and applications*. Academic press.

Sakhaee-Pour, A. (2016). Pore-scale modeling of The Geysers. *Geothermics*, *60*, 58–65. http://doi.org/10.1016/j.geothermics.2015.12.003

Sakhaee-Pour, A., & Bryant, S. L. (2015). Pore structure of shale. *Fuel*, *143*, 467–475. http://doi.org/10.1016/j.fuel.2014.11.053

Sakhaee-Pour, A., & Li, W. (2016). Fractal dimensions of shale. *Journal of Natural Gas Science and Engineering*, *30*, 578–582. http://doi.org/10.1016/j.jngse.2016.02.044

Schull, C. G. (1948). The Determination of Pore Size Distribution from Gas Adsorption Data. *Journal of the American Chemical Society*, *70*(4), 1405–1410. http://doi.org/10.1021/ja01184a034

Seaton, N. A. (1994). Determination of the connectivity of porous solids from nitrogen sorption measurements—III. Solids containing large mesopores. *Chemical Engineering Science*, *49*(11), 1869–1878. http://doi.org/10.1016/0009-2509(94)80071-5

Sing, K. S. W., & Williams, R. T. (2004). Physisorption hysteresis loops and the characterization of nanoporous materials, *22*(10), 773–782. http://doi.org/10.1260/0263617053499032

Skinner, L. ., & Sambles, J. . (1972). The Kelvin equation - A review. *Journal of Aerosol Science*, *3*(3), 199–210. http://doi.org/10.1016/0021-8502(72)90158-9

Swanson, B. F. (1981). A Simple Correlation Between Permeabilities and Mercury Capillary Pressures. *Journal of Petroleum Technology*, *33*(12), 2498–2504. http://doi.org/10.2118/8234-PA

Thommes, M. (2010). Physical adsorption characterization of nanoporous materials. *Chemie-Ingenieur-Technik*, *82*(7), 1059–1073. http://doi.org/10.1002/cite.201000064

Washburn, E. W. (1921). The dynamics of capillary flow. *Physical Review*, *17*(3), 273–283. http://doi.org/10.1103/PhysRev.17.273

Zapata, Y., & Sakhaee-Pour, A. (2016). Modeling adsorption–desorption hysteresis in shales: Acyclic pore model. *Fuel*, *181*, 557–565. http://doi.org/10.1016/j.fuel.2016.05.002

Appendix A

This appendix contains the paper submitted to the journal FUEL, Modeling adsorption-desorption hysteresis in shales: Acyclic pore model.

Fuel 181 (2016) 557–565

Contents lists available at ScienceDirect

Fuel

journal homepage: www.elsevier.com/locate/fuel

Full Length Article

Modeling adsorption–desorption hysteresis in shales: Acyclic pore model

Yuliana Zapata, A. Sakhaee-Pour *

Petroleum and Geological Engineering, The University of Oklahoma, USA

ARTICLE INFO

Article history:
Received 16 February 2016
Received in revised form 1 May 2016
Accepted 2 May 2016
Available online 12 May 2016

Keywords:
Pore-body size
Pore-throat size
Shale

ABSTRACT

Existing conventional measurements face challenges in characterizing transport properties of a shale because they are designed originally for formations with relatively wide pores and high permeability. The integrated analysis of such measurements helps us better understand the connected pore system of a shale formation when they are sensitive to the pore topology and cover a wider range of pore size. Here, we analyze nitrogen adsorption–desorption and mercury intrusion measurements to characterize the pore space of a shale. We determine pore-body size distribution by interpreting adsorption–desorption experiments. We also calculate pore-throat size distribution from mercury intrusion. We adopt the acyclic pore model, which embraces limited pore connectivity, and account for the connected path of the pores at the core scale. Our study distinguishes the pore size relevant to the storage and the flow conductance for the shale.

1. Introduction

Any piece of rock comprises void space and solid grains (non-void regions). In pore-scale modeling [1–6], we analyze the transport properties of the void space at scales smaller than the size of the core (~1 cm) and then relate our analysis to the measurements conducted on the cores. We classify the void space into pore bodies and pore throats and then analyze the interactions between the pores. The pore throat is the narrowest region of the pore space connecting the neighboring pores, whereas the pore body is the wider region of the pore.

Topology of pore space plays an important role in controlling the transport properties [7,8]. Recent advances in acquiring high-resolution images shed light on the pertinent complexity [9,10] but we cannot yet determine the representative size for such images *a priori* [11]. However, the representative size can let us derive a network of the connected pores that can be used for analyzing transport properties at the core scale.

There are few theoretical pore models that account for the effective pore connectivity at the core scale, such as bundle of tubes [12], regular lattice [13], sphere packing [1], multi-type model [14], and acyclic pore model [15–17]. They are physically representative of the pore space because they can capture the transport properties at the core scale. They may not be necessarily representative of the pore connectivity at sub-core scales because we do not test them at those scales. Instead, we usually use core-scale measurements, such as relative permeability [3] and drainage [7,8].

The pore throat is the narrowest region of the pore space connecting adjacent pores and has a dominant effect on the fluid displacement. To determine the pore-throat size distribution for the connected path of the pores at the core scale, we often analyze the drainage data, in which the non-wetting phase displaces the wetting phase. The invasion percolation suggests that the invading fluid displaces the resident fluid when the applied capillary pressure is larger than the critical pressure for the connecting throat. The critical capillary pressure is a functions of the throat curvature that can allow us to determine the pore-throat size distribution using Young–Laplace relation.

The pore volume depends more on the pore-body size. Hence, we can evaluate pore-body size distribution by analyzing adsorbed volume for adsorption–desorption tests. The adsorption begins when the porous medium is exposed to a gas and the molecules adhere to the pore wall. The amount of gas adsorbed is a function of the nature of the solid phase, the gas molecules, the surface area of the solid phase, and the relative pressure.

In an adsorption–desorption test, the variation of adsorbed volume with relative pressure shows hysteresis which is dependent on capillary condensation [18]. In a single conduit, the condensation pressure is a function of the pore-body size, the shape, and the interaction between the fluid and pore wall [19]. In a porous

* Corresponding author.
E-mail address: sakhaee@ou.edu (A. Sakhaee-Pour).

http://dx.doi.org/10.1016/j.fuel.2016.05.002
0016-2361/

medium, the hysteresis is also controlled by pore connectivity [20]. We will take advantage of this dependency for pore space characterization in this study.

Increasing interest in shale formations [21–27] brings up the challenge of estimating former's transport properties, which can be significantly different from those of previously produced formations. As an example, the matrix permeability is usually smaller than 1 μd. The lower permeability can be due to narrower pores and inferior pore connectivity. With this in mind, many people analyzed their pore structures [28–33]. While the conducted studies shed light on the complexity of the pore space, the difference between the pore-body and the pore-throat sizes has not been investigated.

In this paper, we use nitrogen adsorption–desorption isotherms and mercury intrusion capillary pressure measurements to characterize the pore space of a shale. We use acyclic pore model and account for the effective pore connectivity at the core scale [15].

2. Methodology

2.1. Characteristic behavior of a single conduit in adsorption–desorption

We use the Halsey's model to determine the thickness of an adsorbed layer on the pore wall. The Halsey's model relates the thickness of the adsorbed layer to the relative pressure as follows [34]:

$$t = 3.54\left(\frac{-5}{\ln\left(\frac{P}{P_o}\right)}\right)^{1/3} \quad (1)$$

where t is the thickness of the adsorbed layer in Angstroms, P is the gas pressure, and P_o is the saturation pressure.

We can determine the thickness of the adsorbed layer using Halsey's model at small relative pressures (P/P_o). At high relative pressures, Halsey's model is not accurate because it does not account for the condensation and evaporation inside the pore that occur during adsorption and desorption, respectively. The injected gas changes to liquid and fills the capillarity at relative pressures that are higher than the threshold pressure. We determine the threshold relative pressures corresponding to condensation and evaporation as follows [18]:

$$RT\ln\left(\frac{P}{P_o}\right)_{adsorption} = \frac{-\gamma V_{mol}\cos(\theta)}{r_p - t} \quad (2)$$

$$RT\ln\left(\frac{P}{P_o}\right)_{desorption} = \frac{-2\gamma V_{mol}\cos(\theta)}{r_p - t} \quad (3)$$

where R is the gas constant, T is the temperature, γ is the surface tension, $(P/P_o)_{adsorption}$ is the threshold relative pressure corresponding to condensation, $(P/P_o)_{desorption}$ is the threshold relative pressure corresponding to evaporation, V_{mol} is the molar volume of the liquid phase, θ is the contact angle, and r_p is the pore radius. Table 1 lists the pertinent parameters. These relations are relevant to a single conduit, and not to the porous medium.

The thickness of the adsorbed layer on the pore wall is a function of relative pressure (Eq. (1)). The threshold relative pressures relevant to condensation and evaporation are also dependent on the original pore size (Eqs. (2) and (3)). Thus, the original pore size dictates the threshold pressures.

To calculate condensation and evaporation pressures (Eqs. (2) and (3)), we first suppose that the adsorbed layer thickness is negligible ($t = 0$). We then calculate the thickness for the estimated pressures (Eq. (1)). Subsequently, we calculate the pressures using the updated thickness and repeat this process to reach convergence. Fig. 1 presents the results.

The threshold relative pressure can be determined from Fig. 1. In adsorption, there is a sharp increase in relative adsorbed volume at the threshold relative pressure. For instance, the threshold relative pressure is almost equal to 0.55 and 0.87 when the pore size is equal to 3 nm and 20 nm, respectively. There is also a sharp decrease in the adsorbed volume at the threshold relative pressure during desorption. We suppose that the conduit is filled with liquid when the relative pressure is higher than the threshold relative pressure.

We analyze the normalized adsorbed volume (V_n) for a conduit whose pore-body size is smaller than or equal to 130 nm, which is typical for shales. The normalized adsorbed volume is larger for smaller conduits at a given relative pressure (P/P_o). The relative pressure determines the thickness of the adsorbed volume that has a larger volume fraction for narrower conduits. The difference between condensation and evaporation pressures decreases with the conduit size, which shrinks the hysteresis. (Compare the results for 3-nm and 130-nm conduits.) Thus, the difference between adsorption and desorption curves of single a conduit is more significant for narrower conduits.

2.2. Adsorption–desorption measurements

We analyze adsorption–desorption isotherms of shales available in the literature [30,31]. Table 2 lists the pertinent data. We plot the nitrogen isotherms for the shale samples (Fig. 2a and b).

We normalize the measured adsorbed volumes ($V_{exp\text{-}n}$) to analyze the characteristic behavior with relative pressure (Fig. 2c). The hysteresis loop in Fig. 2c suggests the presence of mesopore based on our analysis of a single conduit where condensation and evaporation pressures differ significantly from the bulk saturation pressure. The closure relative pressure is almost equal to 0.45 for all samples and there is no significant difference between the adsorbed volumes determined from adsorption and desorption at relative pressures smaller than this value.

2.3. Acyclic pore model

We use the acyclic pore model [15] to characterize the pore space. There is a unique path between any two points in the model (Fig. 3a) when they are connected [35]. The main feature of the acyclic pore model is that the accessibility of wider pores is not restricted by narrower pores. Narrower pores are accessible from wider throats. Sakhaee-Pour and Bryant [15] showed that the acyclic pore model can capture the drainage experiment when the variation of the capillary pressure with wetting phase saturation exhibits a non-plateau-like trend (Fig. 3b). This allows us to determine the pore-throat size distribution.

Table 1
Input parameters for calculating threshold relative pressures for nitrogen based on Kelvin's model (Eqs. (2) and (3)), and for capillary pressures in mercury intrusion [18].

Nitrogen				Mercury	
R	V_{mol}	γ	θ^o	γ	θ^o
$8.314\left(\frac{J}{K\,mol}\right)$	$3.467\times10^{-5}\left(\frac{m^3}{mol}\right)$	$8.85\times10^{-3}\left(\frac{N}{m}\right)$	0	$487\times10^{-3}\left(\frac{N}{m}\right)$	140

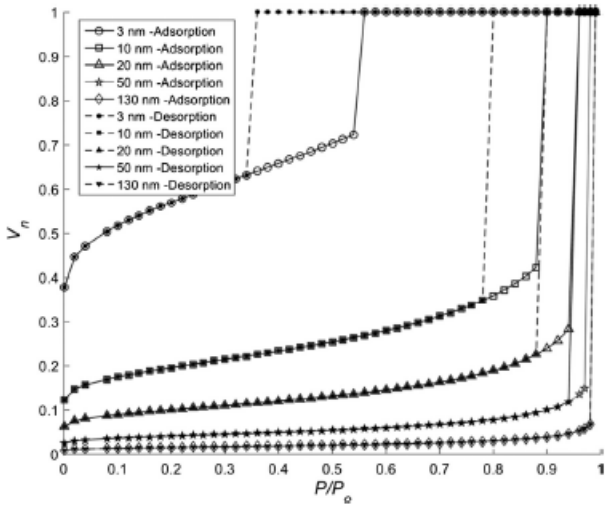

Fig. 1. Variation of the normalized adsorbed volume (V_n) with relative pressure (P/P_o) depends on the pore-body size of the conduit. The normalized volume is for a single circular tube with different diameters (3 nm, 10 nm, 20 nm, 50 nm, and 130 nm).

Table 2
Origin and depth of the shale samples analyzed here. Jiang et al. [30] conducted the nitrogen adsorption–desorption measurements for samples 1–2 and Kuila and Passad [31] did for sample 3–4.

	Sample 1	Sample 2	Sample 3	Sample 4
Origin	Barnett Shale	Barnett Shale	Wyoming Montmorillonite (Swy-2)	Georgia Kaolinite (KGa-1b)
Depth	7610–7756 ft	7610–7756 ft	NA	NA

In this study, we will implement the fundamental assumption that the accessibility of the wider pores is not limited by narrower pores. This will allow us to characterize the pore space not only based on mercury intrusion but also on nitrogen adsorption and desorption.

2.4. Modeling adsorption–desorption using acyclic pore model

Condensation takes places at a higher relative pressure (P/P_o) for wider conduits. The dependency is apparent in Fig. 1 where the sudden increase in the adsorbed volume shifts to a higher relative pressure for wider pores. The same holds true for evaporation during desorption. We have to account for restrictions imposed by narrower pores if they control the accessibility of wider pores.

Narrower pores do not limit the accessibility of wider pores in the acyclic pore model (Fig. 3a). Therefore, we can take into account condensation and evaporation in pores with different pore-body sizes independently in the acyclic model. We can determine the normalized adsorbed volume as follows:

$$V_n\left(\frac{P}{P_o}\right) \propto \sum_i^m L_i V_{n-i}\left(\frac{P}{P_o}\right) \tag{4}$$

where V_n is the normalized adsorbed volume of the porous medium, m is the number of the pore-body size considered, L_i is the normalized length of the conduit size, and V_{n-i} is the normalized adsorbed volume of the conduit. The normalized lengths have to be non-negative to be physically plausible. We can interpret the normalized lengths as weights that relate the characteristic behavior of different conduit sizes to that of the porous medium which imposes the following restrictions:

$$0 \leqslant L_i \leqslant 1 \quad \text{for } i = 1 \text{ to } m \tag{5a}$$

$$\sum_i^m L_i = 1 \tag{5b}$$

To model adsorption–desorption using acyclic pore model, we first determine the normalized adsorbed volume with relative pressure (P/P_o) for each conduit size. We then determine the normalized length corresponding to each size by minimizing the error through iteration. We set the error equal to the difference between the measured and modeled volumes as follows:

$$\text{Error} = |V_{exp-n} - V_n| \tag{6}$$

In each iteration, we change the lengths and evaluate their effects on the error:

$$L_i^* = \text{linespace } (0, 1) \quad \text{for } i = 1 \text{ to } m \tag{7a}$$

$$L_j^* = L_j + \frac{L_i^* - L_i}{m-1} \quad j = 1 \text{ to } m, \quad j \neq i \tag{7b}$$

where L_i and L_j are the old lengths, and L_i^* and L_j^* are the modified lengths. For each size, we pick a length (L_i^*) and the corresponding L_j^* which minimizes the error in each iteration. We use the modified lengths for a new iteration and repeat this process to reach convergence (Fig. 4). We initially suppose that the lengths are equal.

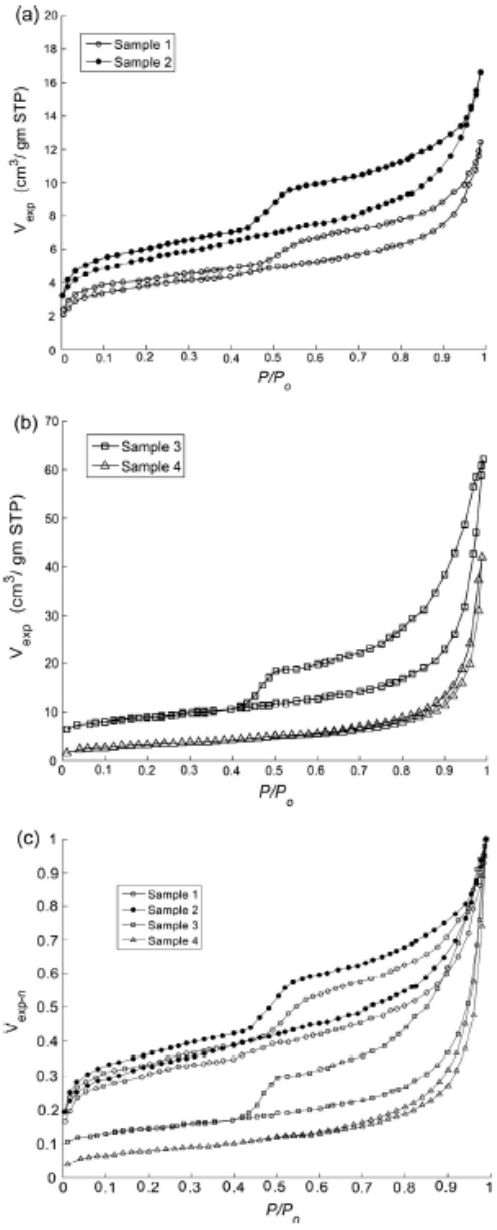

Fig. 2. Nitrogen adsorption–desorption isotherms for (a) samples 1 and 2 [30] and (b) 3 and 4 [31]. (c) The normalize adsorbed volumes show different trends with relative pressure for different samples sample 4 has the minimum hysteresis which suggests that its pore sizes are larger.

The normalized adsorbed volumes are functions of the pore-body size (Fig. 1). This dependency permits us to calculate the pore-body size distribution by accounting for the normalized lengths as follows:

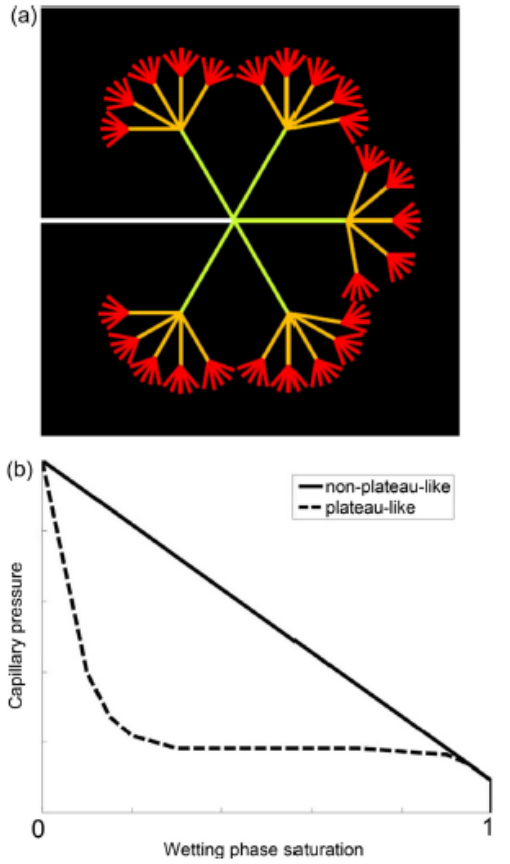

Fig. 3. (a) Acyclic pore model in which there is a single path between any two points in the model [35]. Narrower pores do not limit access to wider pores: red represents the smallest size and white represents the largest size. (b) The acyclic model can capture the non-plateau-like trend of capillary pressure [15–17]. (For interpretation of the references to color in this figure legend, the reader is referred to the web version of this article.)

$$\text{Volume fraction } (d_{p-i}) = \frac{L_i(d_{p-i})d_{p-i}^2}{\sum_i^m L_i(d_p)d_{p-i}^2} \tag{8}$$

where $L_i(d_{p-i})$ is the normalized conduit length whose pore-body size is denoted by d_{p-i}. The nominator is an estimate for the corresponding pore volume and the denominator is an estimate for the total pore volume.

3. Results

We apply the acyclic pore model to characterize the void space of a shale sample. We use the data available in the literature. The linear increase of the capillary pressure with the decreasing wetting phase saturation, shown in Fig. 5, reveals the absence of a plateau-like trend in drainage. This indicates that the acyclic pore model is representative of the pore space. Our objective is to determine the pore-body size for all the samples and the pore-throat

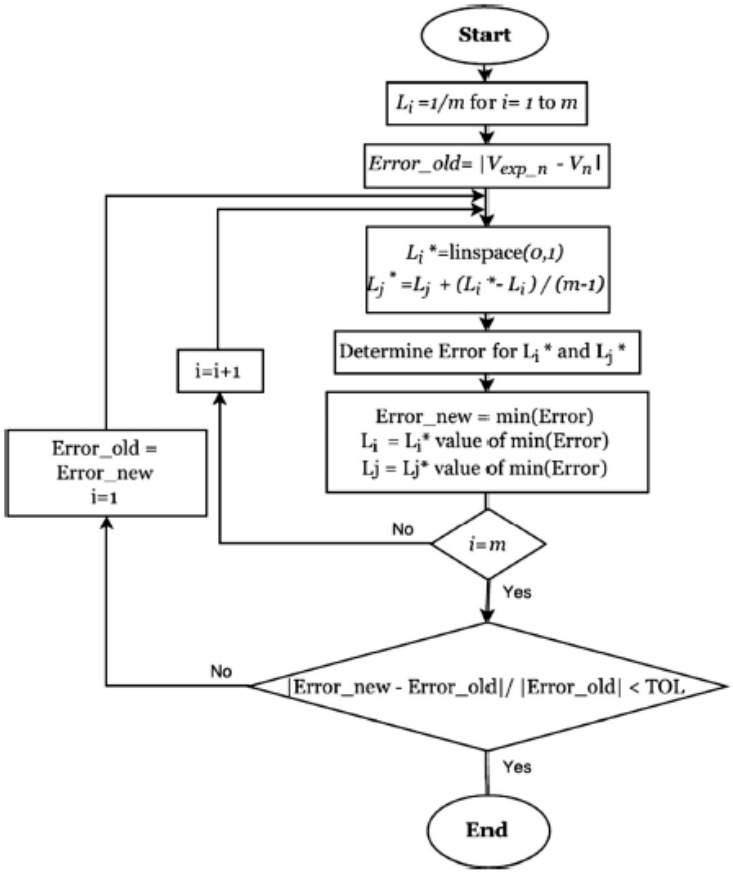

Fig. 4. Flowchart for iteration in acyclic pore model.

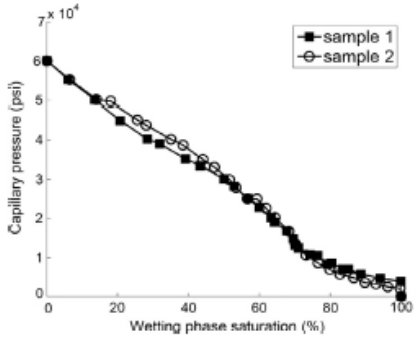

Fig. 5. Mercury intrusion capillary pressures of samples 1 and 2, used for determining pore-throat size distribution, shows a non-plateau-like trend and can be captured using the acyclic pore model.

size only for samples 1 and 2 using the acyclic pore model. This is because mercury intrusion capillary pressure measurements are documented only for samples 1 and 2, whereas nitrogen adsorption and desorption are reported for all the samples.

We characterize the pore space of a shale by capturing nitrogen adsorption and desorption, which allows us to derive the pore-body size distribution (d_p). We also calculate pore-throat size distribution (d_t) via analyzing mercury intrusion capillary pressure measurements. We will compare the results to highlight the difference between the two sizes when both measurements are available.

We have to define the minimum and the maximum pore-body sizes *a priori* to use the acyclic pore model for adsorption–desorption. We take the minimum size equal to 3 nm, which is realistic for shales and valid for the adsorption model (Eq. (1)). We find the maximum pore-body size by determining the error with the pore-body size. Fig. 6 shows the error variation with the maximum pore-body size for different samples. The error is minimum for sample 1 when the maximum pore size is 60 nm; for sample 2 when the maximum pore size is 70 nm; for sample 3 when the maximum pore size is 90 nm; and for sample 4 when the maximum pore size is 110 nm. We will use them to capture the adsorbed volume.

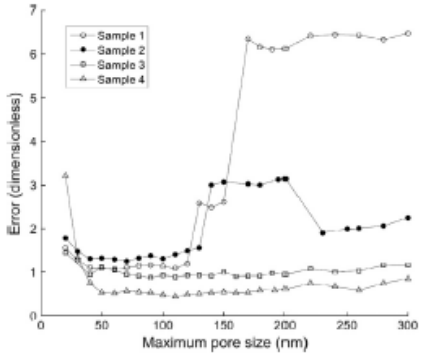

Fig. 6. Variation of error with maximum pore-body size for samples 1, 2, 3 and 4. We use the pore-body size corresponding to the minimum error for each sample.

Error, as defined in Eq. (6), is the difference between the normalized modeled and measured adsorbed volumes. Hence, we can capture the measured adsorbed volume and predict pore-body size distribution more accurately when error becomes smaller. Fig. 6 indicates that the variation of error is very small for larger pores for samples 3 and 4, unlike for samples 1 and 2. This is because the pore volume of the large pore-body sizes is small compared to that of the small pore-body sizes in samples 3 and 4, and this influences the defined error. The pore volume of the large pore-body sizes is more significant in samples 1 and 2 and that is why its effect on error is more notable. We will present the pore-body size distributions of the samples later (Fig. 9).

We now turn to the calculation of the normalized length of each conduit size (L_i). We suppose the lengths are equal initially to model the adsorbed volume and modify them via iteration. Fig. 7 shows the difference between the modeled and the measured normalized volumes for samples 1–4, as an example. The difference is plotted for different iterations with the tube number. We stopped the iterations when the results converge: there is no significant change between the results in iterations 15–20.

We also tested sensitivity to the number of conduits. We determined the difference between the modeled and the measured vol-

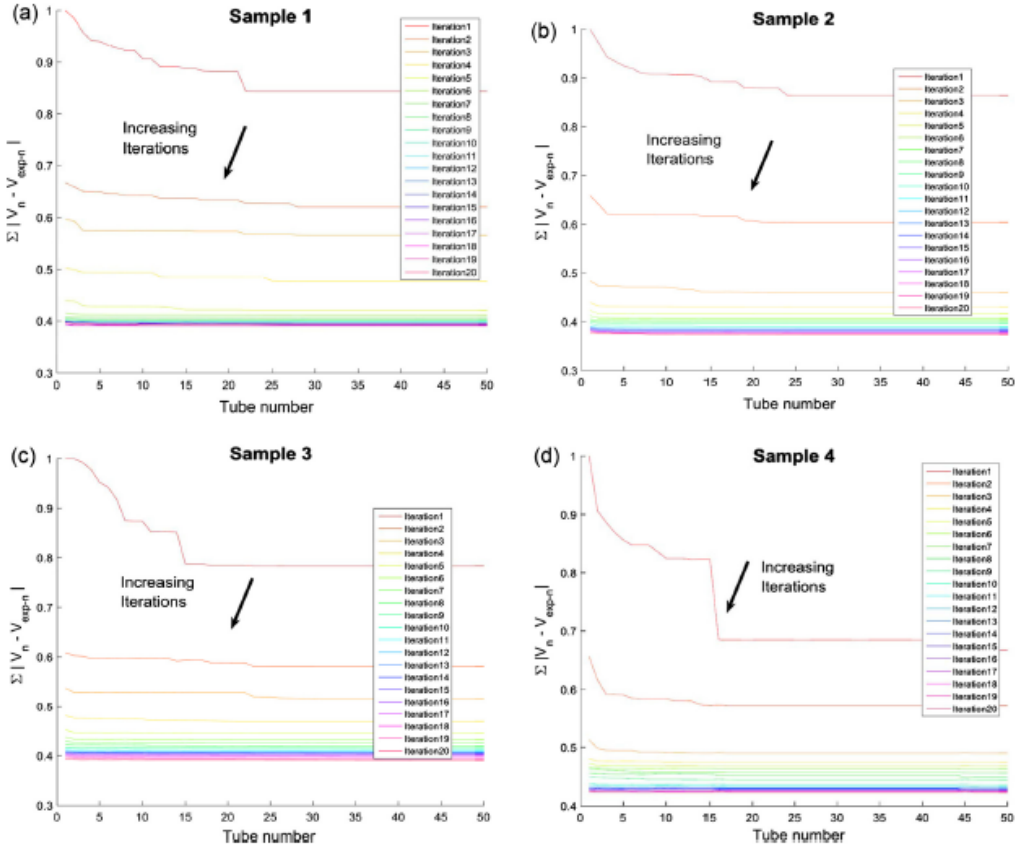

Fig. 7. Effect of the number of iterations on the normalized difference between the modeled and measured adsorbed volumes with the tube number for (a) sample 1, (b) sample 2, (c) sample 3, and (d) sample 4.

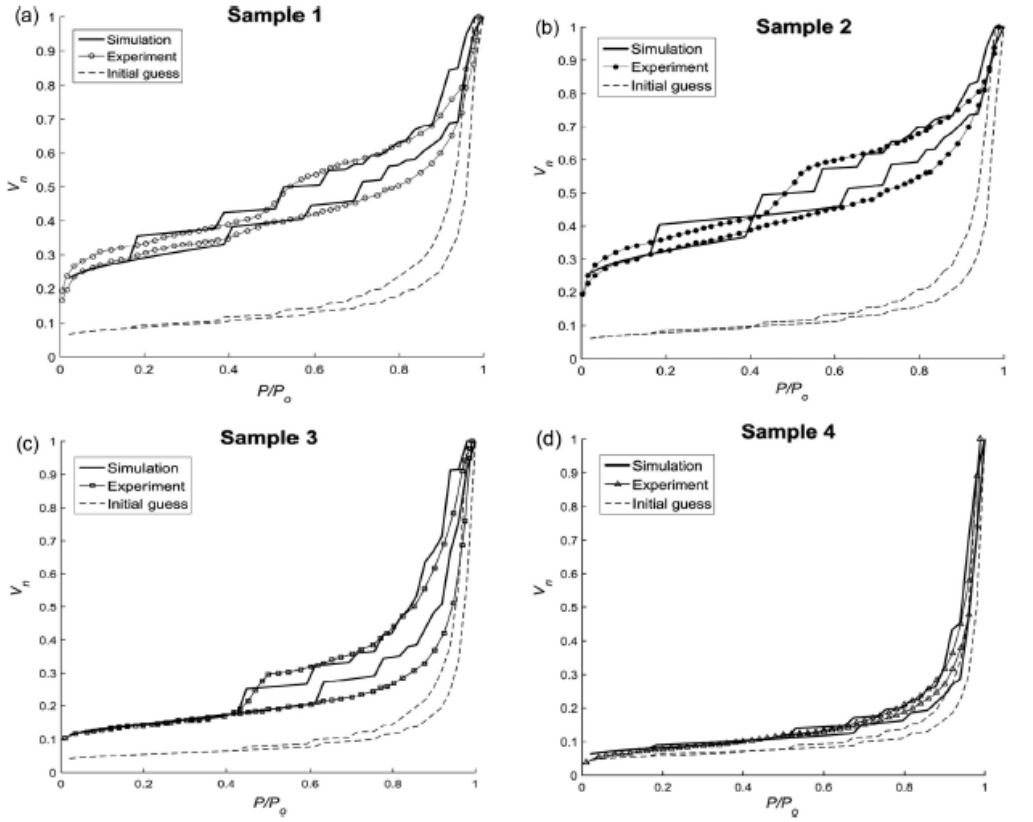

Fig. 8. Measured and simulated nitrogen adsorption–desorption isotherms for samples 1–4.

umes for different numbers of pore-body sizes. We use fifty conduit sizes here because the results do not change significantly with the number of sizes when we have this many conduits. Further, this leads to results with a relatively good resolution.

Next, we plot the adsorbed volume captured using the acyclic pore model by accounting for the normalized length and the normalized adsorbed volume. Fig. 8 shows the experimental adsorption–desorption curves, the modeled isotherms for the converged iteration (simulation), and the initial guess. The modeled adsorbed volumes are improved significantly relative to the initial guess, which is based on equal normalized lengths. There is a hysteresis in the measured adsorbed volume at low relative pressures in samples 1 and 2, which might be because of the fact that the measurements were conducted too fast for the adsorbed volume to leave. Our model assumes there is no hysteresis at low relative pressures.

We calculate the pore-body size distributions of samples 3 and 4 using the acyclic pore model (Fig. 9). For this reason, we account for the normalized length of each conduit size based on Eq. (8). The pore-body size distribution shows a bimodal distribution for sample 3 with maxima close to 30 nm and 80 nm. Sample 4 exhibits a different distribution, whose maximum pore-body size is close to 110 nm.

We compare pore-body and pore-throat size distributions for samples 1–2 whose relative measurements are available in the literature. The former is based on the interpretation of the nitrogen adsorption–desorption and the latter is based on the mercury intrusion. The mercury intrusion results are not available for samples 3 and 4; thus, they are not included here. Fig. 10 quantifies the difference between the two sizes in a single model (acyclic pore model) for pore space characterization. The volume faction of pore-throat is much larger than that of the pore-body size for smaller sizes. The difference becomes less significant for larger sizes. The large volume fraction observed for larger pore-throat size can be relevant to micro fractures that remain open during the mercury intrusion tests because they were conducted with no confining stress. The pore-throat size is more important for understanding flow conductance, whereas the pore-body size plays a more-important role in determining hydrocarbon storage.

The transport properties change significantly when we go from the macroscale, or even the microscale, to the nanoscale. The relevant changes in hydrocarbon transport properties in shales can be classified into storage, which is controlled mainly by the pore body, and fluid displacement, which is dictated mainly by the pore throat. The pore-body size distributions for samples 1 and 2 are

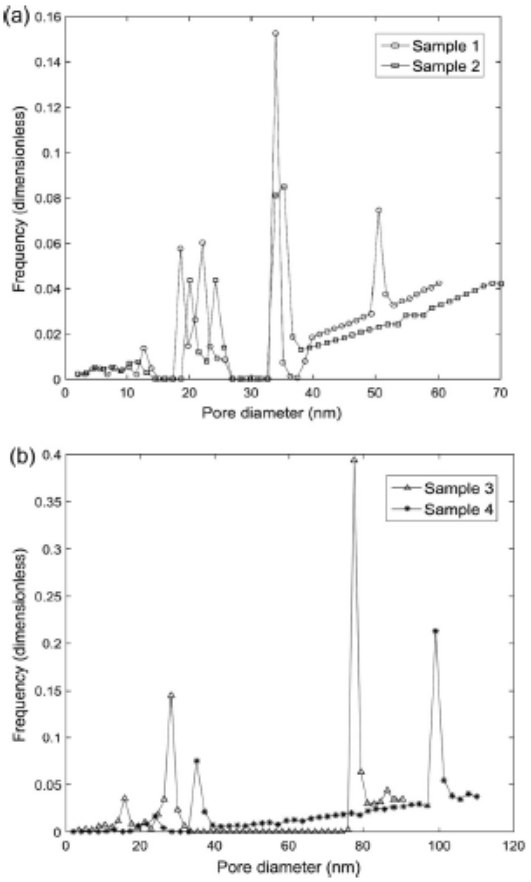

Fig. 9. Pore-body size distributions of (a) samples 1 and 2 and (b) samples 3 and 4, which are determined by modeling the nitrogen adsorption–desorption measurements shown in Fig. 8.

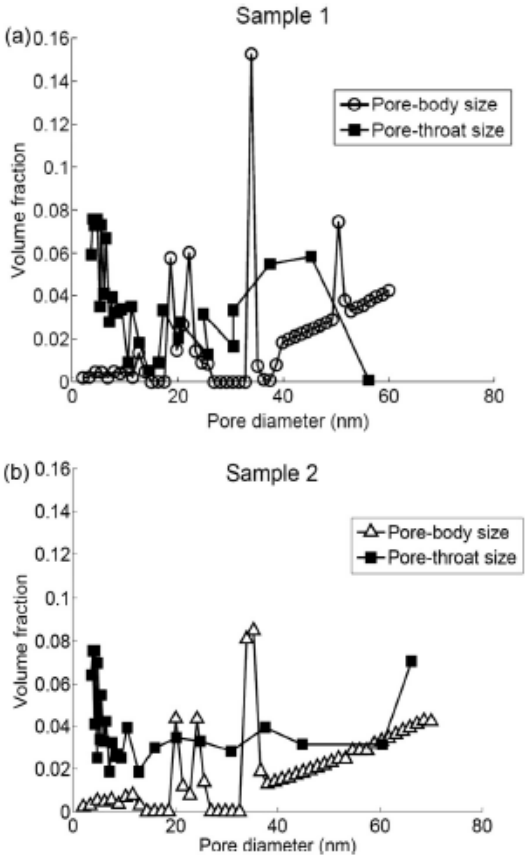

Fig. 10. Pore-body and pore-throat size distributions of samples 1 and 2 that are, respectively, based on the interpretation of the nitrogen adsorption–desorption and mercury intrusion. The two sizes allow us to characterize the pore space using the acyclic pore model [15].

relatively similar, whereas the pore-throat size distributions are different. The similarity suggests that the transport properties controlled by the characteristic size of the bulk volume, such as density, could be relatively similar for the analyzed samples. This demonstrates that, if other governing parameters are identical, the transport properties controlled by the pore throat size can be different. The difference between the changes in predicted transport properties highlights the importance of distinguishing between pore-throat and pore-body sizes for shales.

We can associate the pore volume of a single pore with its pore throat and pore body sizes. There is no general model for relating the two sizes because of the complicated topology of the pore. The two sizes are different, not only because they specify different topological parameters, but also because they control different transport properties. The lack of a general model reveals the difficulty of relating the volume fractions corresponding to equal pore throat and pore body sizes. Fig. 10 reveals that the volume fraction of the pore-body size is smaller than that of the pore-throat size for small sizes, and the difference between the volume fractions becomes less significant as the size increases. Our interpretation is that the transport properties of a significant fraction of the pore volume, whose pore-body sizes have a large volume fraction, are controlled by the small pore throats. Further, the large volume fraction of the small pore-throat size indicates that the corresponding pore volume is significant.

4. Conclusions

Our objective was to characterize the pore space of a shale formation using nitrogen adsorption–desorption and mercury intrusion. Both are dependent on the pore structure; while the former is more appropriate for characterizing the pore body, the latter is for the pore throat. We used the acyclic pore model, which accounts for the limited connectivity in the connected path of the pore space at the core scale, to characterize the pore space. Our model allowed us to capture sorption hysteresis including different adsorption mechanisms, such as the thickening of the adsorbed layer and the capillary condensation. It also enabled us to capture mercury intrusion capillary pressures. This work contributes to the fundamental understanding of the shale formation by quantifying the difference between the characteristic sizes of the pore body and the pore throat. A better understanding of these sizes is critical for predicting the stored volume, controlled by the pore volume, and its hydraulic conductivity, dictated by the pore throat.

References

[1] Bryant SL, Mellor DW, Cade CA. Physically representative network models of transport in porous media. AIChE J 1993;39:387–96.
[2] Sahini M, Sahimi M. Applications of percolation theory. New York: CRC Press; 1994.
[3] Bryant S, Blunt M. Prediction of relative permeability in simple porous media. Phys Rev 1992;46(4):2004.
[4] Hassanizadeh SM, Gray WG. Mechanics and thermodynamics of multiphase flow in porous media including interphase boundaries. Adv Water Res 1990;13 (4):69–186.
[5] Thompson K, Fogler HS. Pore-level mechanisms for altering multiphase permeability with gels. SPE J 1997;2(03):350–62.
[6] Blunt MJ, Bijeljic B, Dong H, Gharbi O, Iglauer S, Mostaghimi P, et al. Pore-scale imaging and modelling. Adv Water Res 2013;51:197–216.
[7] Mousavi MA, Bryant SL. Connectivity of pore space as a control on two-phase flow properties of tight-gas sandstones. Transp Porous Media 2012;94 (2):537–54.
[8] Mousavi MA, Bryant SL. Geometric models of porosity reduction by ductile grain compaction and cementation. AAPG Bull 2013;97(12):2129–48.
[9] Mostaghimi P, Blunt MJ, Bijeljic B. Computations of absolute permeability on micro-CT images. Math Geosci 2013;45(1):103–25.
[10] Bijeljic B, Raeini A, Mostaghimi P, Blunt MJ. Predictions of non-Fickian solute transport in different classes of porous media using direct simulation on pore-scale images. Phys Rev E 2013;87(1):013011.
[11] Ovaysi S, Wheeler MF, Balhoff M. Quantifying the representative size in porous media. Transp Porous Media 2014;104(2):349–62.
[12] Purcell WR. Capillary pressures-their measurement using mercury and the calculation of permeability therefrom. J Pet Technol 1949;1(2):39–48.
[13] Fatt I. The network model of porous media. I. Capillary pressure characteristics. AIME Pet Trans 1956;207:144–59.
[14] Sakhaee-Pour A, Bryant SL. Effect of pore structure on the producibility of tight-gas sandstones. AAPG Bull 2014;98(4):663–94.
[15] Sakhaee-Pour A, Bryant SL. Pore structure of shale. Fuel 2015;143:467–75.
[16] Sakhaee-Pour A. Pore-scale modeling of the geysers. Geothermics 2016;60:58–65.
[17] Sakhaee-Pour A. Fractality of the geysers. Geotherm Energy 2016;4(1):1–10.
[18] Roque-Malherbe RMA. Adsorption and diffusion in nanoporous materials. New York: CRC Press; 2007.
[19] Skinner L, Sambles J. The kelvin equation – a review. J Aerosol Sci 1972;3 (3):199–210.
[20] Sing KSW, Williams RT. Physisorption hysteresis loops and the characterization of nanoporous materials. Adsorpt Sci Technol 2004;22 (10):773–82.
[21] Kethireddy N, Chen H, Heidari Z. Quantifying the effect of kerogen on electrical resistivity measurement in organic-rich source rocks. Petrophysics 2014;55 (3):136–46.
[22] Saneifar M, Aranibar A, Heidari Z. Rock classification in the Haynesville Shale based on petrophysical and elastic properties estimated from well logs. Interpretation 2014;3(1):SA65–75.
[23] Sakhaee-Pour A, Bryant S. Gas permeability of shale. SPE Reservoir Eval Eng 2012;15(04):401–9.
[24] Alfi M, Yan B, Cao Y, An C, Killough JE, Barrufet MA. Microscale porosity models as powerful tools to analyze hydrocarbon production mechanisms in liquid shale. J Nat Gas Sci Eng 2015;26:1495–505.
[25] An C, Alfi M, Yan B, Killough JE. A new study of magnetic nanoparticle transport and quantifying magnetization analysis in fractured shale reservoir using numerical modeling. J Nat Gas Sci Eng 2016;28:502–21.
[26] Yu W, Lashgari HR, Wu K, Sepehrnoori K. CO_2 injection for enhanced oil recovery in Bakken tight oil reservoirs. Fuel 2015;159:354–63.
[27] Ganjdanesh R, Rezaveisi M, Pope GA, Seperhrnoori K. Treatment of condensate and water blocks in hydraulic-fractured shale-gas/condensate reservoirs. SPE J 2016;21:665–74.
[28] Sondergeld C, Ambrose R, Rai C, Moncrieff J. Micro-structural studies of gas shales. In: SPE unconventional gas conference. 2010, Pittsburgh (Pennsylvania, USA): SPE 131771.
[29] Yuan W, Pan Z, Li X, Yang Y, Zhao C, Connell L, et al. Experimental study and modelling of methane adsorption and diffusion. Fuel 2014;117:509–19.
[30] Jiang C, Bryant S, Daigle H. A bundle of short conduits model of the pore structure of gas shale. URTec 2169349; 2015.
[31] Kuila U, Prasad M. Surface area and pore-size distribution in clays and shales. Colorado School of Mines; 2011. SPE 146869.
[32] Clarkson CR, Solano N, Bustin RM, Bustin AMM, Chalmers GRL, He L, et al. Pore structure characterization of North American shale gas reservoirs using USANS/SANS, gas adsorption, and mercury intrusion. Fuel 2013;103:606–16.
[33] Wright M, Court R, Kafantaris FC, Spathopoulos F, Sephton M. A new rapid method for shale oil and shale gas assessment. Fuel 2015;153:231–9.
[34] Halsey G. Physical adsorption on non-uniform surfaces. J Chem Phys 1948;16 (10):931.
[35] Bethe HA. Statistical theory of superlattices. Proc R Soc Lond A 1935;150:552–75.